

# Contents

<b>1</b>	<b>Introduction</b>	<b>1</b>
1.1	Statistical physics . . . . .	2
1.2	This thesis . . . . .	2
1.2.1	Chapter 1 - Thermalization in quantum systems . . . . .	2
1.2.2	Chapter 2 - Symmetry restoration through “registry” . . . . .	3
1.2.3	Chapter 3 - Entanglement entropy of lattice gauge theories. . . . .	4
1.2.4	Chapter 4 - Phase space and efficient learning of deep neural networks. . . . .	4
<b>2</b>	<b>Lyapunov Exponents in the bipartite SYK model]</b>	<b>7</b>
2.1	Introduction. . . . .	8
2.2	Model and methods. . . . .	9
2.2.1	The bipartite SYK model . . . . .	9
2.2.2	Schwinger-Dyson equations . . . . .	10
2.2.3	Real time formalism . . . . .	14
2.3	The four-point function. . . . .	15
2.3.1	Conformal limit . . . . .	17
2.3.2	Numerical analysis for weak and intermediate coupling . . . . .	19
2.4	Results . . . . .	20
2.4.1	Analytics and numerics . . . . .	20
2.4.2	Discussion and Conclusion. . . . .	23
.1	Mathematical consistency of the Lyapunov ansatz . . . . .	24
.2	Recovery of the maximal Lyapunov exponent of the regular SYK . . . . .	25
.3	Finite-size dependence of two-point functions and Lyapunov exponents . .	25
<b>A</b>	<b>Kondo effect in Twisted Bilyaer graphene</b>	<b>29</b>
A.1	Introduction. . . . .	30
A.2	Van Hove singularities in the Bistritzer-MacDonald model. . . . .	32
A.2.1	Particle-hole symmetric Bistritzer-MacDonald model. . . . .	32
A.2.2	Characterization of van Hove singularities in the particle-hole symmetric BM model . . . . .	34

A.3	The Kondo problem. . . . .	36
A.3.1	Poor man's scaling approach . . . . .	38
A.3.2	Numerical Renormalization Group . . . . .	39
A.3.3	Observables . . . . .	41
A.3.4	Limiting cases of the Kondo problem . . . . .	42
A.4	Results and discussion . . . . .	47
A.5	Conclusions . . . . .	50
.1	Locating saddle point positions in the particle-hole symmetric BM model .	51
.2	Mapping from TBG density of states to the NRG Wilson chain . . . . .	52
.3	NRG calculations for an impurity coupled to a conventional log-vHs host .	52

## References

59

# 1

## Introduction

The unifying theme in this thesis is the presence of hidden hyperbolic geometries in strongly interacting systems and their bilayers.

## 1.1. Statistical physics

The primary goal of statistical physics is an exploration of macroscopic quantities and the calculation thereof. Often, the systems we explore are made up of many degrees of freedom, and solving them exactly is impossible. In order to do this, we will assume that the statistical average over all possible states can replace the time average.

One of the main assumptions we make when resorting to statistical calculations instead of fully dynamically solving the system is the principle of *ergodicity*. Ergodicity states that if the system is left to evolve, all accessible states will eventually be realized. This assumption helps us often turn insolvable time integrals into relatively easy and, more importantly, simulation-friendly integrals over the probability distributions of those states. For example, let us say we want to study some volume of gas in a container. At standard temperature and pressure, one liter of oxygen contains around  $3 \cdot 10^{22}$  oxygen molecules moving around the container. Just writing down equations of motion for all molecules would take a very long time, but no practical conclusion can be drawn even if we manage to do it. Hence we turn to the methods of statistical physics.

## 1.2. This thesis

In the introduction, we have covered the basic ideas used later in this thesis. We started with introductory topics in thermodynamics and statistical physics, then moved to a basic introduction to Monte Carlo methods and all the required knowledge to understand our physical system's simulation design and analyze the results. The proceeding section was dedicated to the basics of machine learning, deep learning, and appropriate selection of model, loss function, and minimization method. The last section culminated in a synergy of the previously mentioned topics by combining quantum physics, Monte Carlo methods, and neural networks in neural quantum states that we used to find the ground state and its energy of lattice gauge theories.

### 1.2.1. Chapter 1 - Thermalization in quantum systems

The properties of closed unitary quantum systems and how they exactly thermalize have been one of the leading research questions in statistical physics for a long time. The puzzle is that a thermal ensemble is formally a mixed state, but a mixed state can never arise from unitary evolution from a pure state. The usual answer to how they thermalize is the eigenstate thermalization hypothesis (“ETH”) [? ]. The hypothesis is that in generic quantum theory with many degrees of freedom, most observables

will have a particular form of matrix elements after averaging, and observable will *appear* to thermalize. However, recently [?] showed that ETH has to be taken with care. Even in free field theory, there are operators that *appear* to relax, called operator thermalization hypothesis (OTH). Given a particular no-go condition, the retarded Green's function will typically decay exponentially unless the condition is met. Finding an operator that will satisfy this condition in a general non-integrable theory is challenging but possible. On the other hand, this job is more straightforward in integrable theories due to the extensive number of conserved quantities. We work in the transverse field Ising (TFI) model where we compare a specially designed operator  $\Gamma$  that will satisfy the no-go condition with the Pauli  $\sigma^z$  operator that does not satisfy it. Through the examples, we show the differences and similarities of ETH and OTH and how, despite TFI being an integrable theory,  $\sigma^z$  will relax after the perturbation. Also, we have demonstrated how the no-go condition is a feature of integrability, and any minor deviation from integrability will cause  $\Gamma$  to relax. Our results were later confirmed in [?].

### 1.2.2. Chapter 2 - Symmetry restoration through “registry”

Starting from the simple Wegner gauge theory [? ?], Fradkin and Shenker [?] discovered that when an added matter field is “in the fundamental”, meaning that there is an additional Higgs field that is also governed by  $Z_2$  symmetry as the gauge fields, the Higgs phase and confining phase become one, without a phase transition. In this chapter, we propose a straightforward generalization of their lattice gauge theory that could serve as a candidate for a highly entangled state of matter. We will consider adding multiple  $Z_2$  and  $O(N)$  matter fields on the lattice and gauging them with a common  $Z_2$  field. It will be shown how, in such a case, the Higgs phase becomes separate from the confining phase. It will be characterized by the “registry” order parameter, which turns out to be gauge invariant  $p = 2^{N_{\text{rep}}-1}$  Potts type symmetry, where  $N_{\text{rep}}$  is the number of matter field copies. Interpretation for this type of symmetry is that different matter copies align their vectors locally in strictly parallel or anti-parallel ways, even in the case of continuous  $O(N)$  matter fields. These theories will be studied using Monte-Carlo simulation on a 3D grid using the Metropolis-Hastings algorithm and annealing techniques to improve the convergence near the critical point. From the simulation results, we can discover some unidentified “pseudo-universality” associated with the form of the phase diagram for various numbers of matter field theories.

### 1.2.3. Chapter 3 - Entanglement entropy of lattice gauge theories

Building further on the work from the previous chapter, we will study entanglement entropy in the neural network representation of the above lattice gauge theories, now considered as quantum theories in one lower dimension. Following the seminal work of Carleo and Troeyer [? ], we will construct neural quantum states as the representation of our theory using a variational wavefunction based on Restricted Boltzmann Machines used in Machine Learning. Using ideas from tensor networks that the bond dimension represents the upper bound on the amount of entanglement a state can have, we will postulate that by increasing the number of matter fields, ground state entanglement entropy of our lattice gauge theory will increase as the ratio of hidden vs. visible nodes. We have tested our hypothesis in the case of 2, 3, and 4 matter fields. Within the achievable computational limits, the results are puzzling. Even though increasing the number of variational parameters improved the energy of the ground state, the impact on the entanglement entropy is less than obvious. Curves of entanglement entropy for different system sizes look the same up to the statistical errors.

### 1.2.4. Chapter 4 - Phase space and efficient learning of deep neural networks

This chapter combines some statistical physics insights into machine learning with the computational mechanics of deep random feedforward neural networks. In recent times with the ever-growing amount of available data, neural networks have become one of the de-facto methods for analyzing and processing vast amounts of data [? ]. One of the reasons why these methods became so popular is their ability to express any function with a relatively small number of parameters [? ] and the ease with which this *expressivity* can be increased by adding more depth. This easy fix does not come for free; deep neural networks generally require more training computations. Specifically, they suffer from exploding or vanishing derivatives in optimizing the parameters. The phase space of deep random feedforward neural networks is characterized by the variance of initial weights and the variance of initial bias. Following previous work [? ? ] that demonstrated the existence of order-to-chaos regime change in this phase space, we will examine the behavior of the pre- and post-activations in terms of their distributions and also final accuracy on classification task such as MNIST and CIFAR10. The phase boundary dividing these two regimes is called the edge of chaos (EOC). We demonstrate that for the tanh activation function, not all points along the EOC yield the same learning efficiency. In the case of shallow and narrow neural networks, we define the line of uniformity (LOU), a set of points for which the final layer post-activation values are distributed uni-

formly, i.e., with maximal entropy. We show that moving away to the right from LOU and drastically increasing initial variances means that gradient saturation will start impeding optimization over parameters, i.e., the learning process.





# 2

## Lyapunov Exponents in the bipartite SYK model]

### Attribution

This paper has been previously published as a preprint on arXiv under the title *Operator thermalization vs eigenstate thermalization*, together with Philippe Sabella-Garnier and Koenraad Schalm.[? ]

### Abstract

The Sachdev-Ye-Kitaev (SYK) model shows chaotic behavior with a maximal Lyapunov exponent. In this paper, we investigate the four-point function of a SYK-type model numerically, which gives us access to its Lyapunov exponent. The model consists of two sets of Majorana fermions, called A and B, and the interactions are restricted to being exclusively pairwise between the two sets, not within the sets. We find that the Lyapunov exponent is still maximal at strong coupling. Furthermore, we show that even though the conformal dimensions of the A and B fermions change with the population ratio, the Lyapunov exponent remains constant, not just in the conformal limit where it is maximal, but also in the intermediate and weak coupling regimes.

## 2.1. Introduction

Over the last decade, the Sachdev-Ye-Kitaev (SYK) model has been established as a paradigmatic model accounting for a variety of phenomena ranging from aspects of the physics of black holes to non-Fermi liquids [1–5]. There exist two main variants of this model in the literature: one that is formulated in terms of  $N$  ‘complex’ Dirac fermions, and another one written in terms of  $N$  ‘real’ Majorana fermions. In both cases, the fermions interact via random four-body terms. Irrespective of the formulation, one of the main features of the model is that it exhibits emergent conformal symmetry in the infrared in the strong-coupling and large- $N$  limit. The scaling dimension of the fermion correlation function is given by  $\Delta = \frac{1}{4}$  [6, 7], indicative of strong interactions (for comparison, a free fermion has scaling dimension  $1/2$ ).

There has been a variety of proposals for the creation of SYK-like models in laboratory setups. They range from mesoscopic systems hosting Majorana modes [8, 9], or Dirac fermions in graphene flakes [10, 11], to ultracold atomic systems [12, 13]. A comprehensive review of such possible setups can be found in Refs. [1, 3] and references therein.

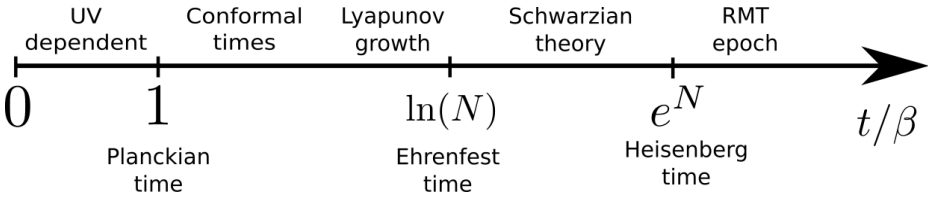


Figure 2.1: The SYK model exhibits multiple characteristic timescales, and with that associated regimes of dynamics. Crucial quantities in distinguishing the different limits are the number of fermions  $N$  and coupling strength  $\beta J$ . This paper studies the region characterized by Lyapunov growth.

The SYK model involves three important time scales, as shown in Fig. 2.1 (henceforth, we measure time  $t$  in units of  $\beta$  and set  $\hbar = k_b = 1$ ). They are called the Planckian time [14–17],  $t_P$ , the Ehrenfest time [18–22],  $t_E$ , and the Heisenberg time  $t_H$ . The shortest time scale,  $t_P$ , is set by the condition  $t_P/\beta \approx 1$ . For times shorter than  $t_P$ , we expect non-universal physics determined by processes at the cutoff scale. For  $t_P < t < t_E$ , the dynamics is governed by the conformal mean-field theory. The chaotic behavior associated with Lyapunov growth [23, 24] in this regime is due to leading irrelevant operators of order  $1/N$  beyond mean-field. The Ehrenfest time is given as  $t_E/\beta \approx \ln N$ , where  $N$  is the number of fermions. The dynamical behavior for  $t_E < t < t_H$  ceases to be described by mean-field theory plus corrections and the associated description is in terms of the Schwarzian theory of black holes. Eventually, there is the Heisenberg time,  $t_H/\beta \approx e^N$ . For times longer than  $t_H$ , the dynamics is described by random matrix theory.

In this paper we study a related model, introduced in Ref. [25, 26], which emerges as

a Majorana variant of the SYK model. It is called the bipartite SYK (or b-SYK) model and, as explained in Sec. 2.2, can be seen as a restricted version of the standard SYK model. Incidentally, Majorana or complex fermion versions of similar models also appear as a natural way to incorporate internal symmetries in SYK models [27–29], or to couple two or more SYK models [30]. We are interested in times shorter than the Ehrenfest time  $t_E$ , and mostly focus on the chaotic behavior. Furthermore, we are interested in studying the growth of the four-point function not just in the full conformal limit at strong coupling, but also at intermediate and weak couplings, as these might be relevant for experimentally achievable values of coupling and temperature, as the b-SYK model has been shown to be realizable in a laboratory by straining a real material in Ref.[26].

We show that the Lyapunov exponent is maximal in the conformal limit, just as for the SYK model [6, 23, 24]. The behavior of the chaos exponent for a general number of majorana fermions in the  $A$  and  $B$  subsets of the b-SYK at finite coupling is unanswered in the existing literature and is the subject of the present study. We use numerical methods to solve the Schwinger-Dyson and Bethe-Salpeter equations that are needed to extract the Green functions and Lyapunov exponents, respectively. We find that the b-SYK model ratio of  $A$  and  $B$  majoranas does not influence the Lyapunov exponent for all values of coupling.

The present paper is organized as follows: In Sec. 2.2, we introduce the b-SYK model and comment on how it is related to more common variants of SYK models. In Sec. 2.2.2 we discuss the two-point functions in and away from the conformal limit. In Sec. 2.3, we compute the four-point function and introduce the equations that allow us to extract the Lyapunov exponents. In Sec. 2.4, we numerically find the Lyapunov exponents and show how they depend on the population balance between  $A$  and  $B$  Majorana fermions.

## 2.2. Model and methods

### 2.2.1. The bipartite SYK model

The bipartite SYK (b-SYK) model consists of two sets of Majorana fermions, labelled  $A$  and  $B$ , with random interactions between pairs of  $A$  and pairs of  $B$  fermions. Interactions between only  $A$  or only  $B$  fermions are absent, and the fermion parity in both the  $A$  and  $B$  subsets is conserved. The Hamiltonian reads

$$H = \frac{1}{4} \sum_{i,j,\alpha,\beta} J_{ij\alpha\beta} \gamma_i^A \gamma_j^A \gamma_\alpha^B \gamma_\beta^B. \quad (2.1)$$

To distinguish the two sets of fermions we use latin indices  $i, j$  for the  $A$ -flavor Majorana fermions ( $\gamma_i^A$ ), and greek indices  $\alpha, \beta$  for  $B$ -flavor Majorana fermions ( $\gamma_\alpha^B$ ).

We allow for  $N_A$  Majorana fermions of the  $A$ -type and  $N_B$  of the  $B$ -type. The ratio  $\kappa = N_A/N_B$  accounts for the relative size of the two sets. The couplings  $J_{ij\alpha\beta}$  are random and only act between sets, not within each set. Concerning the normalization of the interaction strength, we follow the convention of Gross and Rosenhaus [31] and choose the variance of the coupling constant to be <sup>1</sup>

$$\langle J_{ij\alpha\beta} J_{i'j'\alpha'\beta'} \rangle = \frac{J^2(N_A + N_B)}{N_A^2 N_B^2} \delta_{i,i'} \delta_{j,j'} \delta_{\alpha,\alpha'} \delta_{\beta,\beta'}.$$

In this work, we will define  $N$  as the geometric mean of  $N_A$  and  $N_B$ ,  $N = \sqrt{N_A N_B}$ . We can then rewrite  $\frac{N_A + N_B}{N_A^2 N_B^2} = (\sqrt{\kappa} + \frac{1}{\sqrt{\kappa}})/N^3$ , which makes the symmetry between  $\kappa$  and  $1/\kappa$  apparent. For clarity, this convention differs from the one used in Refs. [25, 26], where  $\langle J_{ij\alpha\beta} J_{i'j'\alpha'\beta'} \rangle = \frac{J^2}{2\sqrt{N_A N_B}^3} \delta_{i,i'} \delta_{j,j'} \delta_{\alpha,\alpha'} \delta_{\beta,\beta'}$ .

The model has a well-defined large- $N$  conformal limit upon taking  $N_A, N_B \rightarrow \infty$ , keeping the ratio  $\kappa = \frac{N_A}{N_B}$  fixed. Rather than a single scaling dimension as in the standard SYK model, the two sets of Majorana fermions,  $A$  and  $B$ , have distinct scaling dimensions,  $\Delta_A$  and  $\Delta_B$ . These depend on the parameter  $\kappa$ , cf. Ref. [25], as

$$\kappa = \frac{2\Delta_A}{1 - 2\Delta_A} \left( \frac{1}{\tan(\pi\Delta_A)} \right)^2. \quad (2.2)$$

For  $\kappa = 1$  we find  $\Delta_A = \Delta_B = 1/4$ , just like in the standard SYK model, although the model is still different since not all Majorana fermions interact with each other. For other values of  $\kappa$ , both scaling dimensions interpolate between 0 and  $1/2$  while always fulfilling  $\Delta_A + \Delta_B = 1/2$ . Tunable scaling dimensions have also been found in other variants of the SYK model e.g Ref. [28, 32–34].

## 2.2.2. Schwinger-Dyson equations

For the later numerical analysis to follow, one main input is required, the Green functions. Hence we recapitulate the crucial steps in solving the model in the large- $N$  limit via the associated Schwinger-Dyson equations. For more details on the procedure in the present context see e.g. Ref. [25]. In this part of the paper, the focus is more on finding a reliable numerical implementation of the Green function that allows to access the conformal limit. The crucial step is to consider the mean-field or large- $N$  limit. Compared to the conventional SYK model, we have to modify the limit slightly. We take  $N_A, N_B \rightarrow \infty$  while keeping  $\kappa = N_A/N_B$  fixed. As in the conventional case, there is one order  $O(1)$  diagram per species of fermions, the so-called ‘melon’ diagrams. These are shown in Fig. 2.2. The diagrams contain the coupling  $J^2$  to all orders and exhibit an emergent conformal symmetry in the infrared, as explained below.

<sup>1</sup>note that this is the  $q=2, f=2$  limit of Ref. [31]

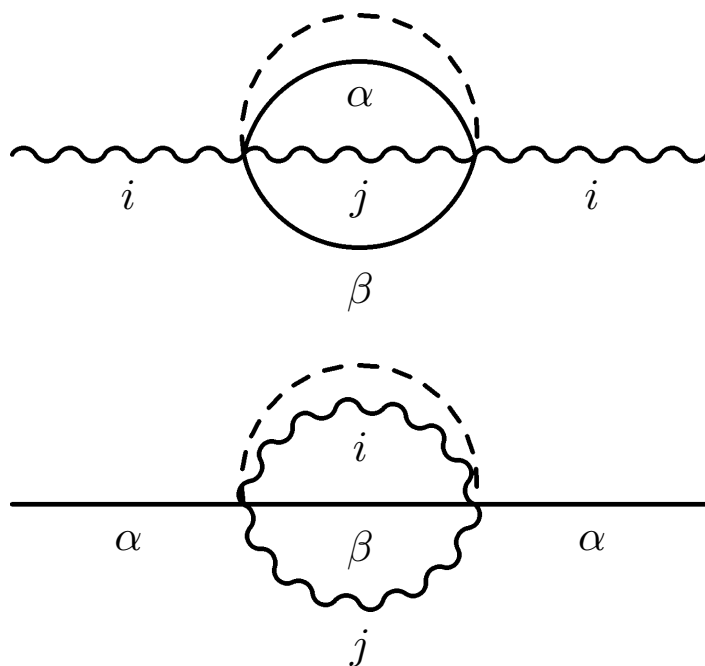


Figure 2.2: The diagrams that contribute to the self energies of A (top) and B (bottom) Majoranas in the large- $N$  limit. Wiggly (solid) lines denote A (B) Majorana propagators, and the dotted line indicates a quenched disorder average  $\sim J^2$ .

### Imaginary time formalism

The discussion of equilibrium properties of the Schwinger-Dyson (SD) equations is easiest carried out in the finite-temperature imaginary time formalism. The inverse temperature is denoted as  $\beta = 1/T$  ( $\hbar = k_B = 1$ ). For the two species, the SD equations read

$$G^{A/B}(i\omega_n) = \frac{1}{-i\omega_n - \Sigma^{A/B}(i\omega_n)}, \quad (2.3)$$

where the respective self energies are given by

$$\Sigma_A(\tau) = \frac{J^2}{2} \left(1 + \frac{1}{\kappa}\right) G^A(\tau) \left(G^B(\tau)\right)^2, \quad (2.4a)$$

$$\Sigma_B(\tau) = \frac{J^2}{2} (1 + \kappa) G^B(\tau) \left(G^A(\tau)\right)^2. \quad (2.4b)$$

Here  $\omega_n = (2n+1)\pi T$  for integer  $n$  are the fermionic Matsubara frequencies, whereas  $\tau$  denotes imaginary time. The Fourier transform between Matsubara frequencies and imaginary time is defined according to

$$G(i\omega_n) = \int_0^\beta e^{i\omega_n \tau} G(\tau) d\tau, \quad (2.5a)$$

$$G(\tau) = \frac{1}{\beta} \sum_{\omega_n} e^{-i\omega_n \tau} G(i\omega_n). \quad (2.5b)$$

One can show analytically that the finite temperature imaginary time Green functions are given by [25]

$$\begin{aligned} G^A(\tau) &= a \operatorname{sgn}(\tau) \left( \frac{\pi}{\beta \sin\left(\frac{\pi\tau}{\beta}\right)} \right)^{2\Delta_A}, \\ G^B(\tau) &= b \operatorname{sgn}(\tau) \left( \frac{\pi}{\beta \sin\left(\frac{\pi\tau}{\beta}\right)} \right)^{2\Delta_B}, \end{aligned} \quad (2.6)$$

where for a given  $\kappa$ , the scaling dimensions  $\Delta_A$  and  $\Delta_B$  are related according to Eq. (2.2).

As far as the overall constants  $a$  and  $b$  are concerned, it is found that only the product  $ab$  is uniquely determined, and not the numbers  $a$  and  $b$  themselves. When we assume that the self energy dominates over the free propagator, we can use the conformal ansatz in equations Eq. (2.4) and (2.3) for each of the  $A$  and  $B$  flavors respectively. Naively, we would expect that the two equations are sufficient to constrain the two unknowns  $a$  and  $b$  respectively, but it turns out the two equations are identical,

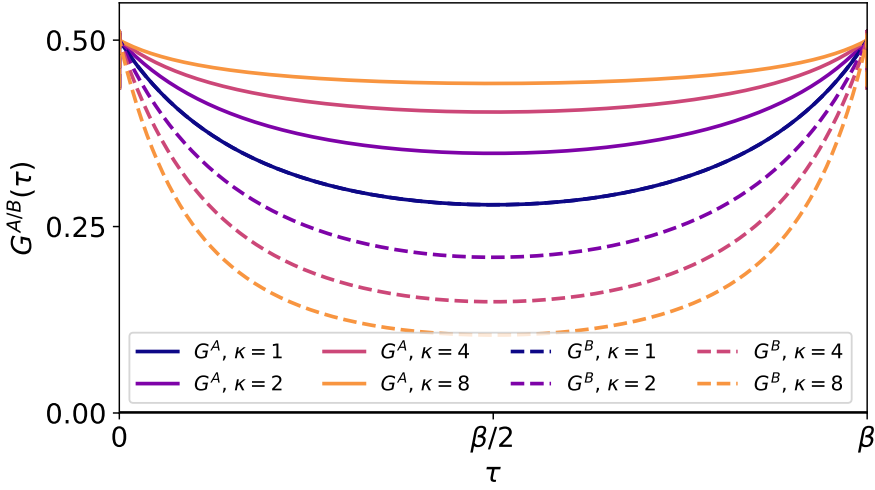


Figure 2.3: Finite temperature Majorana Green functions  $G^{A/B}(\tau)$  for  $\beta J = 10$  and several values of  $\kappa$ . Taking  $\kappa \rightarrow 1/\kappa$  exchanges the  $A$  and  $B$  species, hence we plot only  $\kappa \geq 1$ .

and only the product is constrained. The result is

$$\frac{1}{a^2 b^2} = \frac{J^2}{2} \left(1 + \frac{1}{\kappa}\right) 2\pi \frac{\cot(\pi\Delta_A)}{1 - 2\Delta_A} \quad (2.7)$$

$$= \frac{J^2}{2} (1 + \kappa) 2\pi \frac{\cot(\pi\Delta_B)}{1 - 2\Delta_B}. \quad (2.8)$$

However, in the real system, at short times, the conformal ansatz is no longer valid, and the free propagator wins over, and  $G^{A/B}(\tau)$  should go as  $\frac{1}{2}\text{sgn}(\tau)$ . This is sufficient to uniquely constrain the short time dynamics of the model.

Numerically, we solve the Schwinger-Dyson equations in a self-consistent manner by repeated evaluation of the Green functions and self-energies paired with an iteration on an imaginary time grid running from 0 to  $\beta$ . Eqs. (2.5a), (2.5b) and similarly for the self-energies here are recast in the form of discrete Fourier transforms, for which there are efficient numerical algorithms such as Fast Fourier transform. To achieve convergence, we use a weighted update of the Green functions according to  $G^{new} = \frac{x}{-i\omega_n - \Sigma} + (1-x)G^{old}$  with a small mixing parameter  $x$ ; here  $\Sigma(i\omega_n)$  denotes the associated self-energy calculated from  $G^{old}$  of the previous iteration.

In Fig. 2.3 we show the Majorana Green functions  $G^{A/B}(\tau)$  for  $\beta J = 10$  and for a variety of values of  $\kappa$ . By fitting the numerically obtained  $G^{A/B}$  to Eq. (2.6) one can see that the scaling dimensions indeed match the conformal results. Overall, we find excellent agreement in the region  $0 \ll \tau \ll \beta$ .

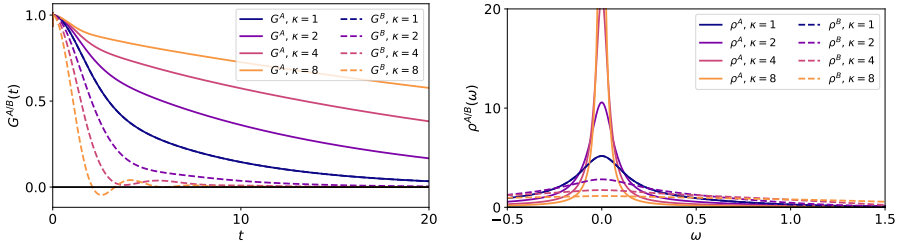


Figure 2.4: *Left panel:* the retarded Green functions  $G_R^{A/B}(t)$  for  $\beta J = 10$ . The characteristic decay time-scale is set by the conformal dimension  $\Delta_{A,B}$ . *Right panel:* the corresponding spectral functions, showing a strong dependence on  $\kappa$ .

### 2.2.3. Real time formalism

The main goal of this paper is to numerically study the out-of-time-ordered correlator (OTOC) in the b-SYK model. To compute it, we need the real time retarded Green function as input. We first note the Dyson equation for the retarded propagator [27, 29, 35, 36]

$$(G^R(\omega + i\delta))^{-1} = \omega + i\delta - \Sigma^R(\omega + i\delta). \quad (2.9)$$

We drop the  $A/B$  labels, unless explicitly required. The spectral decomposition for the Green functions reads:

$$G(z) = \int_{-\infty}^{\infty} \frac{d\Omega}{\pi} \frac{\rho(\Omega)}{z - \Omega}, \quad (2.10a)$$

$$\rho(\omega) = -\text{Im}\{G^R(\omega + i\delta)\}. \quad (2.10b)$$

Since the self energies are well defined in imaginary time according to Eq. (2.4), we can use Eqs. (2.5a), (2.5b) and (2.10) to express  $\Sigma(i\omega_n)$  in terms of the spectral function. The analytical continuation is then done by replacing  $i\omega_n \rightarrow \omega + i\delta$ , resulting in

$$\Sigma_B^R(\omega + i\delta) = \frac{J^2}{2}(1+\kappa) \int \int \int \frac{d\omega_1}{\pi} \frac{d\omega_2}{\pi} \frac{d\omega_3}{\pi} \rho_A(\omega_1) \rho_A(\omega_2) \rho_B(\omega_3) \frac{[n(\omega_1)n(\omega_2)n(\omega_3) + n(-\omega_1)n(-\omega_2)n(-\omega_3)]}{\omega + i\delta - \omega_1 - \omega_2 - \omega_3} \quad (2.11)$$

where  $n(\omega)$  is the Fermi-Dirac distribution function. The expression for  $\Sigma_A$  is obtained by changing  $A \leftrightarrow B$ , and  $\kappa \leftrightarrow 1/\kappa$ . In principle, the Schwinger-Dyson equations can be solved iteratively for  $G_{A/B}^R(\omega)$  and  $\rho^{A/B}(\omega)$ . However, nested numerical integration is both highly inefficient in its usage of resources and numerically unstable. Instead, it is beneficial to rewrite it using the following decomposition which allows an implementation using only the discrete Fourier transform, cf. Refs. [29, 37].



We can express the self energies as

$$\Sigma_A^R(\omega + i\delta) = -i \frac{J^2}{2} \left(1 + \frac{1}{\kappa}\right) \int_0^\infty dt e^{i(\omega + i\delta)t} \left[ n_A^+(t) n_B^+(t) n_B^+(t) + n_A^-(t) n_B^-(t) n_B^-(t) \right] \quad (2.12)$$

$$\Sigma_B^R(\omega + i\delta) = -i \frac{J^2}{2} (1 + \kappa) \int_0^\infty dt e^{i(\omega + i\delta)t} \left[ n_B^+(t) n_A^+(t) n_A^+(t) + n_B^-(t) n_A^-(t) n_A^-(t) \right], \quad (2.13)$$

where the function  $n_{A/B}^\pm(t)$  is defined through

$$n_{A/B}^\pm(t) = \int_{-\infty}^\infty \frac{d\omega_1}{\pi} e^{-i\omega_1 t} \rho_{A/B}(\omega_1) n(\pm\omega_1). \quad (2.14)$$

The retarded Green function and the corresponding spectral functions obtained from the real-time/frequency iteration of the above SD equations are shown in Figure 2.4.

## 2.3. The four-point function

We now turn our attention to the four-point correlators of the b-SYK model, and in particular to the out-of-time-ordered correlators (OTOCs). Before we have a look into OTOCs themselves, we first discuss conventional four-point functions. In imaginary time, a general four-point function of Majoranas has the form [31]

$$\mathcal{F}(\tau_1, \tau_2, \tau_3, \tau_4) = \frac{1}{N^2} \sum_{ijkl} \left\langle \gamma_i^{f_1}(\tau_1) \gamma_j^{f_2}(\tau_2), \gamma_k^{f_3}(\tau_3) \gamma_l^{f_4}(\tau_4) \right\rangle. \quad (2.15)$$

The disorder averaging and the large- $N$  limit taken together restrict the contributions to the four-point functions to stem from what are known as ladder diagrams. These can be categorized into four channels, depending on the flavors of the incoming and outgoing pairs of fermion propagators: AA-AA, AA-BB, BB-AA, and BB-BB. A diagram with  $n + 1$  rungs can be obtained from a diagram with  $n$  rungs by convolution with a kernel [23]. In the vicinity of the Ehrenfest time  $t_E$ , this can be cast as a self-consistent Bethe-Salpeter equation according to

$$\mathcal{F}_{\alpha\beta}(\tau_1, \tau_2, \tau_3, \tau_4) = \int d\tau d\tau' K_{\alpha\gamma}(\tau_1, \tau_2, \tau, \tau') \mathcal{F}_{\gamma\beta}(\tau, \tau', \tau_3, \tau_4) \quad (2.16)$$

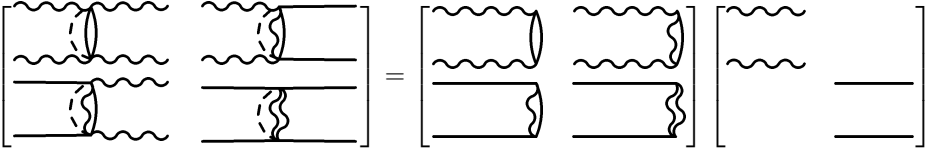


Figure 2.5: Diagrammatic representation of the matrix-kernel equation (2.16) at first order. Repeated application of the kernel  $K$  generates all terms in  $\mathcal{F}$

where  $\gamma$  is summed over, and the Kernel matrix is given as (in imaginary time and a regularized version in real time respectively)

$$K_{\alpha\gamma}(\tau_1 \cdots \tau_4) = -J^2 \begin{pmatrix} \frac{1}{2}(1 + \frac{1}{\kappa}) G^A(\tau_{13}) G^A(\tau_{24}) (G^B(\tau_{34}))^2 & (1 + \frac{1}{\kappa}) G^A(\tau_{13}) G^A(\tau_{24}) (G^A(\tau_{34}) G^B(\tau_{34})) \\ (1 + \kappa) G^B(\tau_{13}) G^B(\tau_{24}) (G^A(\tau_{34}) G^B(\tau_{34})) & \frac{1}{2}(1 + \kappa) G^B(\tau_{13}) G^B(\tau_{24}) (G^A(\tau_{34}))^2 \end{pmatrix} \quad (2.17)$$

$$K_{\alpha\gamma}^R(t_1 \cdots t_4) = J^2 \begin{pmatrix} \frac{1}{2}(1 + \frac{1}{\kappa}) G_R^A(t_{13}) G_R^A(t_{24}) (G_W^B(t_{34}))^2 & (1 + \frac{1}{\kappa}) G_R^A(t_{13}) G_R^A(t_{24}) (G_W^A(t_{34}) G_W^B(t_{34})) \\ (1 + \kappa) G_R^B(t_{13}) G_R^B(t_{24}) (G_W^A(t_{34}) G_W^B(t_{34})) & \frac{1}{2}(1 + \kappa) G_R^B(t_{13}) G_R^B(t_{24}) (G_W^A(t_{34}))^2 \end{pmatrix} \quad (2.18)$$

The indices  $\alpha, \beta, \gamma$  refer to the flavors of the Majorana propagators on the external legs. For example,  $F_{00}$  refers to the AA-AA scattering and  $F_{10}$  refers to BB-AA scattering. A diagrammatic representation of the matrix-kernel equation (2.16) is shown in Fig. 2.5.

Quantum chaos is characterized by the Lyapunov exponent. Instead of looking at the real time version of Eq. (2.15), we consider a regularized version according to

$$F_{ab}(t_1, t_2) = \frac{1}{N^2} \sum_{a,b} \overline{\text{Tr}\{\sqrt{\rho}[\gamma_a(t_1), \gamma_b(0)] \sqrt{\rho}[\gamma_a(t_2), \gamma_b(0)]\}}. \quad (2.19)$$

This regularized OTOC has the thermal density matrix  $\rho$  of the thermal average split evenly between pairs of Majorana operators, and brackets  $[\cdot, \cdot]$  denote commutators. In diagrammatic language this means that the four point function is evaluated on a double-fold Schwinger-Keldysh contour with insertions of the Majorana operators as shown in Fig. 2.6.

This is a regularization not of the UV, but of the IR. Details on which of the many possible choices of regularization and Schwinger-Keldysh contour one might pick can be found in Ref. [38]. The key point is that for massless theories, which the SYK universality class belongs to, all different regularizations give the same exponential growth, even though the values of the actual OTOCs may differ. For the choice in Eq. (2.19), the four point function in question will be generated by ladder diagrams with retarded or advanced Green functions on the rails, and so-called Wightman functions  $G^W(t) = G(\frac{\beta}{2} + it)$  on the rungs. Formally, the latter are obtained by an analytic continuation of the imaginary time Green function noted in Sec. 2.2.2. This

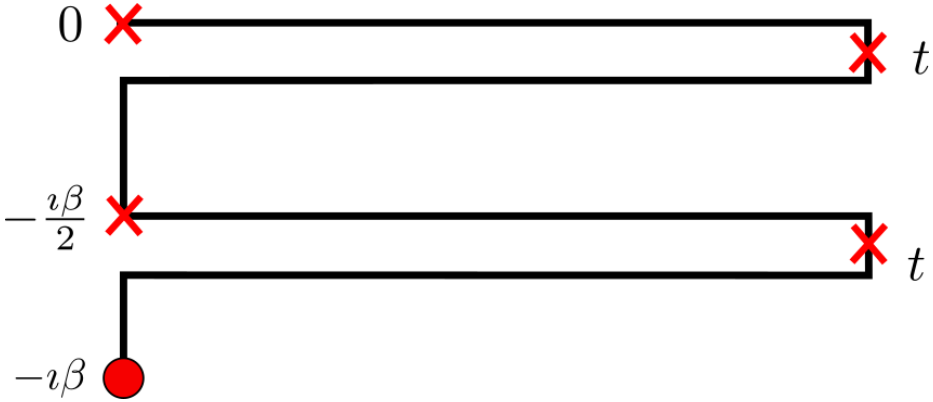


Figure 2.6: Schwinger-Keldysh contour with two temporal folds (excursions to time  $t$ ) and Majorana operator insertions (red crosses) that represents the regularized OTOC in Eq. (2.19).

analytic continuation can be performed with the use of the spectral decomposition, also known as a Hilbert transform. In total, one obtains the result

$$G^W(\omega) = \frac{\rho(\omega)}{2 \cosh \frac{\beta\omega}{2}}. \quad (2.20)$$

The late time exponential growth of the OTOC [24] can then be fit to the Lyapunov ansatz

$$\mathcal{F}_{\alpha\beta}(t_1, t_2) = e^{\lambda_{\alpha\beta} \frac{(t_1+t_2)}{2}} f_{\alpha\beta}(t_{12}). \quad (2.21)$$

As opposed to the standard SYK model, each of the four different scattering channels might ostensibly have its own Lyapunov exponent. It turns out that this is not the case. A detailed technical explanation involving the consistency of the Lyapunov ansatz with a single exponent  $\lambda$  is presented in Appendix .1.

A simple qualitative argument for a single Lyapunov exponent is that the scattering channels all feed back into each other. The AA-AA scattering amplitude also passes through the AA-BB channel and then back into the BB-AA channel. This imposes a sense of self-consistency between the scattering channels, which in turn forces them to have the same late time Lyapunov growth.

### 2.3.1. Conformal limit

Taking the ansatz that all four Lyapunov exponents  $\lambda_{\alpha\beta}$  are the same, *i.e.*  $\lambda_{\alpha\beta} = \lambda$  allows us to make an ansatz for the growth equation. First, we will notice that the equations for  $f_{00}$  and  $f_{10}$  decouple, and we get the same equations for the other pair  $f_{01}$  and  $f_{11}$ . In the conformal limit, following [6] we can use the conformal mapping

to obtain the retarded and Wightman Green functions from Eqs. (2.6) to get

$$G_R^A(t) = 2a \cos(\pi\Delta_A) \left( \frac{\pi}{\beta \sinh \frac{\pi t}{\beta}} \right)^{2\Delta_A} \quad (2.22a)$$

$$G_W^A(t) = a \left( \frac{\pi}{\beta \cosh \frac{\pi t}{\beta}} \right)^{2\Delta_A}, \quad (2.22b)$$

and likewise for the  $B$ - fermions. The growth ansatz can also be made in analogy with the regular SYK case:

$$\begin{pmatrix} f_{00}(t_{12}) \\ f_{10}(t_{12}) \end{pmatrix} = \begin{pmatrix} a \mathcal{C}_a \left( \frac{\pi}{\beta \cosh(t_{12} \frac{\pi}{\beta})} \right)^{2\Delta_a+h} \\ b \mathcal{C}_b \left( \frac{\pi}{\beta \cosh(t_{12} \frac{\pi}{\beta})} \right)^{2\Delta_b+h} \end{pmatrix} e^{h(t_1+t_2) \frac{\pi}{\beta}} \quad (2.23)$$

It can be noted that Eq. (2.23) is a way of rewriting Eq. (2.21) in a way that is convenient for the conformal limit calculation.  $\mathcal{C}_a$  and  $\mathcal{C}_b$  are hitherto undetermined constants. The equations one needs to solve are then (the factors of  $\frac{\pi}{\beta}$  have been chosen appropriately so that they scale away)

$$e^{h(t_1+t_2)} f_{00}(t_{12}) = \frac{J^2}{2} (1 + \frac{1}{\kappa}) \int dt_3 dt_4 \left[ G_R^A(t_{13}) G_R^A(t_{24}) G_W^B(t_{34})^2 f_{00}(t_{34}) + \right. \\ \left. 2G_R^A(t_{13}) G_R^A(t_{24}) G_W^B(t_{34}) G_W^A(t_{34}) f_{10}(t_{34}) \right] e^{h(t_3+t_4)} \quad (2.24a)$$

$$e^{h(t_1+t_2)} f_{10}(t_{12}) = \frac{J^2}{2} (1 + \kappa) \int dt_3 dt_4 \left[ G_R^B(t_{13}) G_R^B(t_{24}) G_W^A(t_{34}) G_W^B(t_{34}) f_{00}(t_{34}) + \right. \\ \left. 2G_R^B(t_{13}) G_R^B(t_{24}) G_W^A(t_{34})^2 f_{10}(t_{34}) \right] e^{h(t_3+t_4)} \quad (2.24b)$$

The way to solve these equations is to first represent the  $t_{34}$  part as an inverse fourier transform, which factorizes the integral into a function that depends only on  $t_3$  and another function that depends only on  $t_4$ , which can be separately integrated. One can express the fourier transforms for powers of hyperbolic sines and cosines as analytic continuations of the Euler Beta function

$$\int_{-\infty}^{\infty} dt e^{i\omega t} \frac{1}{(\cosh t)^\alpha} = 2^{\alpha-1} B\left(\frac{\alpha-i\omega}{2}, \frac{\alpha+i\omega}{2}\right), \quad (2.25a)$$

$$\int_{-\infty}^{\infty} dt e^{i\omega t} \frac{\theta(t)}{(\sinh t)^\alpha} = 2^{\alpha-1} B\left(\frac{\alpha-i\omega}{2}, 1-\alpha\right). \quad (2.25b)$$

The result then is that

$$\mathcal{C}_a = \mathcal{M} (\mathcal{C}_a + 2\mathcal{C}_b) \quad (2.26a)$$

$$\mathcal{C}_b = \mathcal{M}' (2\mathcal{C}_a + \mathcal{C}_b), \quad (2.26b)$$

where

$$\mathcal{M} = \frac{(1 - 2\Delta_A) \sin(2\pi\Delta_A)}{\pi} \frac{(\Gamma(1 - 2\Delta_A))^2 \Gamma(2\Delta_A + h)}{\Gamma(2 - 2\Delta_A + h)} \quad (2.27)$$

$$\mathcal{M}' = \frac{(1 - 2\Delta_B) \sin(2\pi\Delta_B)}{\pi} \frac{(\Gamma(1 - 2\Delta_B))^2 \Gamma(2\Delta_B + h)}{\Gamma(2 - 2\Delta_B + h)} \quad (2.28)$$

The equations Eqs. (2.26) only have a trivial solution  $\mathcal{C}_A = \mathcal{C}_B = 0$  if either of the scaling dimensions are 0 or  $\frac{1}{2}$ , i.e, the  $\kappa = 0$  and  $\kappa \rightarrow \infty$  models are not chaotic in the strictly conformal limit.

For any other intermediate  $\kappa$ , even infinitesimally small, Eqs. (2.26) permit a solution if

$$\det \begin{bmatrix} \mathcal{M} - 1 & 2\mathcal{M} \\ 2\mathcal{M}' & \mathcal{M}' - 1 \end{bmatrix} = 0. \quad (2.29)$$

We have solved this equation for  $h$  and the solution found is always  $h = 1$  for any value of  $\kappa$ . This means that for the b-SYK model, it is always possible to increase the coupling and lower the temperature sufficiently that the system always has a maximal Lyapunov exponent  $\lambda = \frac{2\pi}{\beta}$ .

For realistic couplings and not too low temperatures, one needs to observe the behavior of the Lyapunov exponent including non-conformal corrections to the Green function by perturbatively including the  $\iota\omega$  term in the Dyson equation. If the correction to the Kernel is  $\delta K_R$ , and if we compute all the eigenvalues in the conformal limit and call them  $k(h)$ , then we can Taylor-expand  $k(h)$  about  $h = 1$ . The point is now that  $h = 1$  gives eigenvalue  $k(h) = 1$ , so we say that

$$k(1 + \delta h) = 1 + k'(1) \delta h \quad (2.30)$$

Thus in order to keep the kernel having eigenvalue 1, the correction

$$\begin{aligned} \langle \delta K_R \rangle &= \delta h k'(1) \\ \implies \delta h &= \frac{\langle \delta K_R \rangle}{k'(1)} \end{aligned} \quad (2.31)$$

is the first non-conformal correction to the lyapunov exponent.

### 2.3.2. Numerical analysis for weak and intermediate coupling

Rather than take this complicated approach, the weak and intermediate coupling limits can be analysed numerically. We can bring the kernel equation into the concise

form

$$f_{\alpha\beta}(\omega) = \left| G_R^\alpha(\omega + i\frac{\lambda}{2}) \right|^2 (\tilde{K}_{\alpha 0} * f_{0\beta} + \tilde{K}_{\alpha 1} * f_{1\beta}), \quad (2.32)$$

where additionally a Fourier transform was performed. The ansatz function  $f_{\alpha\beta}(\omega')$  is analyzed in frequency space, see below. We also denote the shifted frequency  $\tilde{\omega} = \omega + i\frac{\lambda}{2}$  that enters in the retarded Green function. The latter is obtained from the regular retarded Green function  $G_R(\omega + i\delta)$  that is calculated in Sec. 2.2.3 by use of the Fourier shift theorem. The symbol  $\star$  in Eq. (2.32) indicates a convolution with the ansatz function  $f_{\gamma\beta}(\omega)$ . The part of the kernel elements  $\tilde{K}_{\alpha\gamma}(\omega)$  that contains the Wightman Green functions is given by

$$\tilde{K}_{\alpha\beta}(\omega) = J^2 \begin{pmatrix} \frac{1}{2}(1 + \frac{1}{\kappa}) \mathfrak{F}[(G_W^B(t))^2] & (1 + \frac{1}{\kappa}) \mathfrak{F}[(G_W^B(t) G_W^A(t))] \\ (1 + \kappa) \mathfrak{F}[(G_W^B(t) G_W^A(t))] & \frac{1}{2}(1 + \kappa) \mathfrak{F}[(G_W^A(t))^2] \end{pmatrix} \quad (2.33)$$

where  $\mathfrak{F}[\cdot]$  represents the Fourier transformation.

Finally, note that Eq. (2.32) can be thought of as an eigenvalue problem for the ansatz  $f_{\alpha\beta}(\omega)$  in frequency space  $\omega$  with a block structure  $\alpha, \beta$  due to the different kernel matrix blocks according to

$$\begin{bmatrix} f_{00}(\omega) \\ f_{10}(\omega) \\ f_{01}(\omega) \\ f_{11}(\omega) \end{bmatrix} = \begin{bmatrix} |G_R^A(\tilde{\omega})|^2 \tilde{K}_{00}(\omega - \omega') & |G_R^A(\tilde{\omega})|^2 \tilde{K}_{01}(\omega - \omega') & 0 & 0 \\ |G_R^B(\tilde{\omega})|^2 \tilde{K}_{10}(\omega - \omega') & |G_R^B(\tilde{\omega})|^2 \tilde{K}_{11}(\omega - \omega') & 0 & 0 \\ 0 & 0 & |G_R^A(\tilde{\omega})|^2 \tilde{K}_{00}(\omega - \omega') & |G_R^A(\tilde{\omega})|^2 \tilde{K}_{01}(\omega - \omega') \\ 0 & 0 & |G_R^B(\tilde{\omega})|^2 \tilde{K}_{10}(\omega - \omega') & |G_R^B(\tilde{\omega})|^2 \tilde{K}_{11}(\omega - \omega') \end{bmatrix} \quad (2.34)$$

On the finite frequency grid, the convolution operations naturally translate to matrix multiplications. For a solution of  $f_{\alpha\beta}$  to exist, the matrix operator needs to have 1 as its largest eigenvalue [6, 18, 23]. This is equivalent to saying that Eq. (2.21) is the correct form for the late time behavior of the OTOC, and the Lyapunov exponent is thus fixed uniquely.

## 2.4. Results

### 2.4.1. Analytics and numerics

We now present and discuss the results of our numerical calculations and compare to analytically known limits. This will reveal some limitations of the numerical method rooted in numerous finite size effects. From the analysis in the preceding chapter, we know that the Lyapunov exponent  $\lambda$  is maximal in the conformal limit for all values of  $\kappa$ . Furthermore, we confirmed numerically that for  $\kappa = 1$ , then  $\lambda$ , as a function of

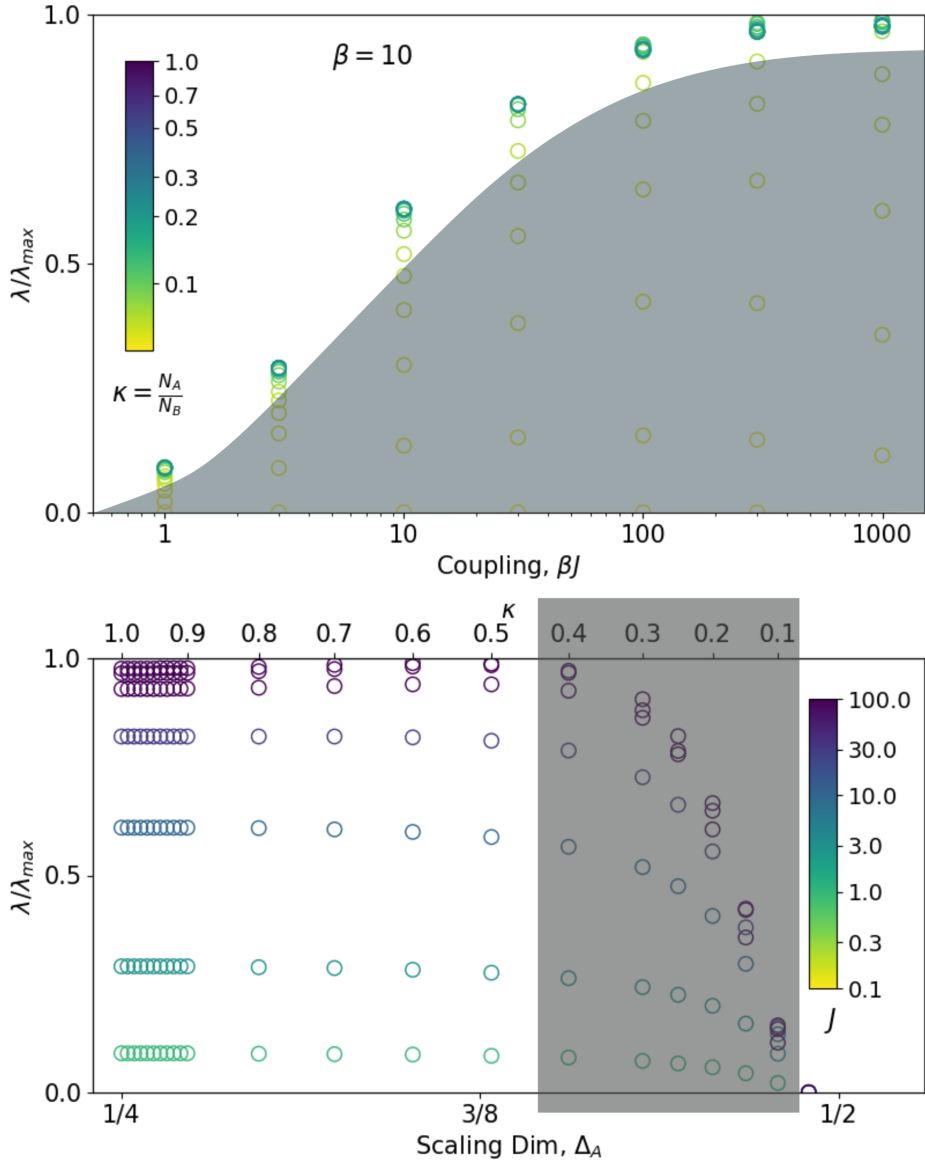


Figure 2.7: (Left) The Lyapunov exponent as a function of the coupling strength  $\beta J$  and for various values  $\kappa = N_A/N_B$ . For  $\kappa > 0.7$  and  $\beta J \gtrsim 300$  the b-SYK model saturates the quantum chaos bound of  $\lambda = 2\pi/\beta$ . The special case  $\kappa = 1$  has identical  $\lambda$  as in the SYK model. (Right) The Lyapunov exponent as a function  $\kappa$  for various values of  $\beta J$ . We find that when  $\kappa \gtrsim 0.5$  then  $\lambda$  is independent of  $\kappa$ . The apparent downturn of the Lyapunov exponent, as a function of  $\kappa$ , can be attributed to the inability of the numerics when the scaling dimensions for the two species are drastically different. In both figures, the grayed out region shows where the numerical results should not be trusted.

$J$ , has identical behavior as in the normal SYK model. This behavior has previously been studied in Ref. [6].

Numerically, we studied the behavior of  $\lambda$  as a function of  $\beta J$  for various values of  $\kappa = N_A/N_B$ . Figure 2.7 (left) shows the Lyapunov exponent  $\lambda$  as a function of the coupling  $\beta J$  for a variety of values of  $\kappa$ . The different values of  $\kappa$  are encoded in the color scale. We do not show values of  $\kappa > 1$  because they are equivalent to those for  $1/\kappa$  by symmetry upon exchange of the species. The figure suggests that  $\lambda$  for all curves with  $\kappa \approx 1$  are approximately the same. Smaller values of  $\kappa$  seem to differ significantly in their value of  $\lambda$  (the gray shaded region is affected by strong finite size effects and the results should not be trusted, see discussion in Appendix .3). We find that the numerics allows to approach the fully conformal limit of the model, meaning  $\lambda/\lambda_{\max}$  approaches 1 in the strong coupling limit for values  $\kappa \approx 1$ , in agreement with our analytical results.

For intermediate couplings  $\beta J$ , which is beyond the reach of any analytical treatment, numerical calculations are more accurate [6]. Similar to Ref. [6], we find for this regime of  $J$ , that the Lyapunov exponent decreases following a  $1/J$  behavior. In total, we find that for values of  $0 \ll \kappa \leq 1$ , the Lyapunov exponent is mostly agnostic to the population ratio  $\kappa$ .

It is instructive to analyze the  $\kappa$  dependence in more detail. In Figure 2.7 (right) we fix  $J$  and vary  $\kappa$  (or  $\Delta_A$ ). We observe that the value of  $\lambda$  is *independent* of  $\kappa$  up to some characteristic value of  $\kappa$ , after which it begins to decline (grey area). We argue that the downturn in  $\lambda$  is an artifact of the numerical method we are using. Essentially we are seeing a finite-size effect in that the time/frequency discretization in the numerics is not fine enough. We have checked for isolated points that the gray area can be pushed upon increasing the resolution.

An immediate question that follows is why the finite-size effects appear only for values of  $\kappa$  away from 1. This can be understood upon considering the scaling dimensions as a function of  $\kappa$ : decreasing  $\kappa$  increases the spread in scaling dimensions of the  $A$  and  $B$  Majorana fermions. This implies that one has to keep track of two time/and frequency scales that we need to accurately capture with our numerical frequency-grid where the scaling limit of one of the two is pushed to larger times. Getting a good resolution of that requires a finer frequency grid at small frequencies. When  $\kappa$  deviates too much from 1 this becomes increasingly costly in terms of time/frequency steps. An extended discussion of the finite size effects in the two-fermion Green function is given in Appendix .3.



### 2.4.2. Discussion and Conclusion

Having established that the Lyapunov exponent is independent of  $\kappa$ , we can compare our results to a similar model presented in Ref. [39]. In that case, the authors find a Lyapunov exponent in the conformal limit which can be tuned by adjusting the relative populations of the different species of fermions. In our model, we find a stark contrast to this behavior. Instead, we find that our model's Lyapunov exponent is completely impervious to the relative number of fermion species. In the conformal limit, aside from showing this result in an explicit analytical calculation, we can motivate the result in a physical way, as a sort of "proof by contradiction". If for example, the  $A$ -flavor Majorana had a smaller Lyapunov exponent, the diagrams contributing to its four point function proceed by a pathway in which they scatter into two  $B$ -flavor Majoranas, which would then propagate with the greater Lyapunov exponent, before finally scattering back into two  $A$ -flavor Majoranas. This forces both flavors to have exactly the same exponent, and a mathematical version of this argument is presented in Appendix .1.

The two-point function of the Majoranas are characterized by their scaling dimension, which is quite sensitive to the relative population ratio  $\kappa$ , so one would expect that the four-point function as characterized by the Lyapunov exponent would depend on  $\kappa$  as well, but we have shown conclusively that this is not the case for cases of strong, intermediate and weak coupling, which is quite surprising. An interesting future direction of study would be to consider what deformations should be introduced to the theory in order to have a different Lyapunov exponent for the two flavors of Majoranas.

The present work on the calculation of the Lyapunov exponent in the b-SYK model shows that the features of emergent conformal symmetry and maximal quantum chaos of the SYK model are quite robust to the couplings obeying additional internal symmetries. Besides the particular model considered here, there are many setups where parity, charge, spin, or general flavor symmetries of the underlying fermions carry over to the interaction matrix elements [1, 3, 28, 29, 34]. The methods used here readily carry over to those models and can be applied to the calculation of Lyapunov exponents and, in general, to the analysis of Bethe-Salpeter equations.

## acknowledgments

We acknowledge discussions with Y. Cheipesh, A. Kamenev, K. Schalm, M. Haque, and S. Sachdev. Extensive discussions with D. Stanford about the conformal limit of the OTOC are also acknowledged. SP thanks E. Lantagne-Hurtubise, O. Can, S. Sahoo, and M. Franz for many useful discussions related to SYK models and holography. This work is part of the D-ITP consortium, a program of the Netherlands

Organisation for Scientific Research (NWO) that is funded by the Dutch Ministry of Education, Culture and Science (OCW). SP received funding through the European Research Council (ERC) under the European Union's Horizon 2020 research and innovation program.

## Author Contributions

A.S.S and M.F contributed equally to this work.

### .1. Mathematical consistency of the Lyapunov ansatz

The following short consideration for the diagram piece  $\mathcal{F}_{00}$  shows why we expect only one ‘global’ Lyapunov exponent for all scattering channels. The other components of the four-point function can be treated with exactly the same argument. The starting point is

$$\begin{aligned} \mathcal{F}_{00}(t_1, t_2) = \int dt_3 dt_4 K_{00}(t_1, t_2, t_3, t_4) \mathcal{F}_{00}(t_3, t_4) \\ + K_{10}(t_1, t_2, t_3, t_4) \mathcal{F}_{10}(t_3, t_4) \end{aligned} \quad (35)$$

where we use the definition

$$\begin{aligned} t_{1,2} &= t \pm \frac{1}{2} t_{12} \\ t_{3,4} &= \tilde{t} \pm \frac{1}{2} t_{34}. \end{aligned} \quad (36)$$

The factors of a half were included to keep the area element invariant under this transformation,  $dt_3 dt_4 = d\tilde{t} dt_{34}$ . After some algebra, for the ansatz  $f_{00}$  one finds

$$\begin{aligned} f_{00}(t_{12}) = J^2 \frac{1}{2} \left( 1 + \frac{1}{\kappa} \right) \int d\tilde{t} dt_{34} G_A^R(t_{13}) G_A^R(t_{24}) \left[ \frac{1}{\kappa} (G_B^W(t_{34}))^2 e^{\lambda_{00} \tilde{t} - \lambda_{00} t} f_{00}(t_{34}) + \right. \\ \left. (G_A^W(t_{34}) G_B^W(t_{34})) e^{\lambda_{10} \tilde{t} - \lambda_{00} t} f_{10}(t_{34}) \right] \end{aligned} \quad (37)$$

Now we Fourier transform according to

$$G_A^W(t_{34}) = \int \frac{d\omega_a}{2\pi} e^{-i\omega_a t_{34}} G_A^W(\omega_a). \quad (38)$$

If we calculate a sample term  $f_{00}$  to illustrate the point,

$$\begin{aligned} f_{00}(\omega) = J^2 \frac{1}{2} \left( 1 + \frac{1}{\kappa} \right) \int dt_{12} e^{i\omega t_{12}} \int d\tilde{t} \int dt_{34} \int \frac{d\omega_a}{2\pi} e^{-i\omega_a (t - \tilde{t} + \frac{1}{2}(t_{12} - t_{34}))} \int \frac{d\omega_b}{2\pi} e^{-i\omega_b (t - \tilde{t} - \frac{1}{2}(t_{12} - t_{34}))} \\ G_A^R(\omega_a) G_A^R(\omega_b) \int \frac{d\omega_c}{2\pi} \int \frac{d\omega'}{2\pi} e^{-i(\omega_c + \omega') t_{34}} \left[ \tilde{K}_{00}(\omega_c) f_{00}(\omega') e^{\lambda_{00} \tilde{t} - \lambda_{00} t} + \tilde{K}_{10}(\omega_c) f_{10}(\omega') e^{\lambda_{10} \tilde{t} - \lambda_{00} t} \right] \end{aligned} \quad (39)$$

we notice that there are three time integrations that result in delta functions, but 4  $t$ -like variables. In the case of the first term in the square brackets, since it only appears in the combination  $(\tilde{t} - t)$ , this eliminates a variable, and there are sufficient constraints to make it only depend on  $\omega$  variables. However, in the new term coming from flavor-mixing of the b-SYK, this is not true any more. This is a signal of a breakdown of the ansatz Eq. (2.21). We thus see that for consistency we must impose that  $\lambda_{00} = \lambda_{10}$ . By repeating the argument for the other components of  $\mathcal{F}$ , it can be shown that all Lyapunov components should be the same,  $\lambda_{ij} = \lambda$ , and that there is only one Lyapunov exponent governing the behavior of the model.

## 2. Recovery of the maximal Lyapunov exponent of the regular SYK

At  $\kappa = 1$ , the numerics reflect that the Lyapunov exponent of the model is the same as the maximal value of regular SYK. This can be understood by looking at the kernel Eq. (2.17). At  $\kappa = 1$ , the scaling dimensions of both the  $A$  and  $B$  majoranas become  $\frac{1}{4}$ , and hence  $G^A(\tau) = G^B(\tau) \equiv G(\tau)$ , the 2 point function of regular SYK. The kernel then factorizes into the product of a function of the four imaginary times, and a constant matrix.

$$K(\tau_1 \cdots \tau_4) = -J^2 G(\tau_{13}) G(\tau_{24}) G(\tau_{34})^2 \begin{pmatrix} 1 & 2 \\ 2 & 1 \end{pmatrix} \quad (40)$$

The constant matrix in question has eigenvalues  $-1$  and  $+3$ . The latter eigenvalue makes the kernel mathematically the same as the one for regular SYK, and hence the Lyapunov exponent should be the same. Furthermore, it is for this reason that the special case of  $\kappa = 1$  allows the kernel to be diagonalized in the basis of the conformal blocks labeled by  $h$ . For  $\kappa \neq 1$ , the four components of the kernel transform differently under transformations of the conformal group.

## 3. Finite-size dependence of two-point functions and Lyapunov exponents

In this section, we briefly comment on the sensitivity of the two-point function to the finite-size cut-offs introduced when numerically solving the Schwinger-Dyson equations for the b-SYK model. To solve the coupled b-SYK equations (Eq. (2.9) and below), we discretize the semi-infinite positive timeline by introducing a long time cut-off  $T$  and a finite number of time steps  $N$  inbetween. This introduces a discretized time-step  $\Delta t = T/N$  and frequency step  $\Delta \omega = 2\pi/T$ . To avoid the discontinuities at  $\omega = 0$  and  $t = 0$ , we choose a time grid that is  $t_n = \Delta t \cdot (n + 1/2)$ , and similarly for the frequency grid.

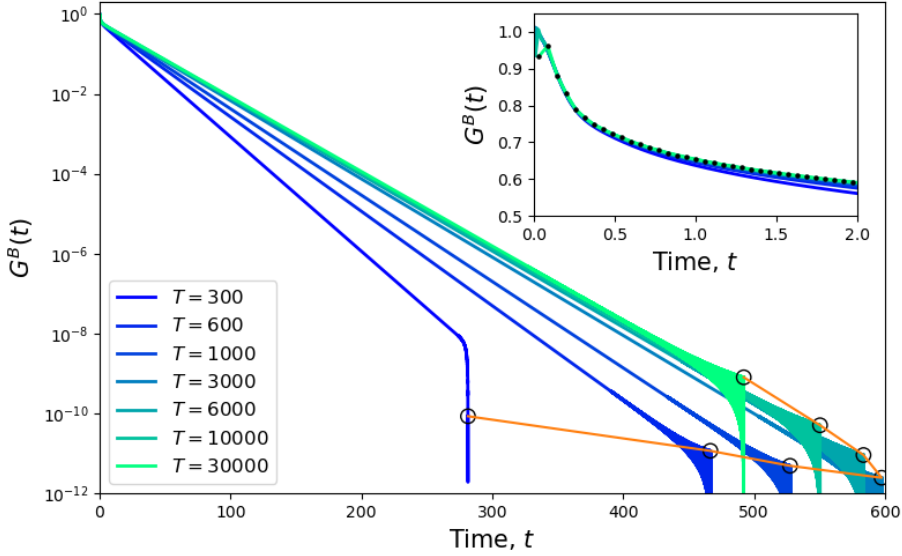


Figure 8: The Green function  $G^B(t)$  for  $\kappa = 0.3$ ,  $\beta = 10$ ,  $J = 10$ . The number of discretization points is fixed to  $N = 2^{19}$  and the length of the time-grid  $T$  is varied. The figure shows that increasing  $T$  gives a better estimate of the decay-time for the Green function, but if  $T$  is taken to be too high, numerical accuracy of the Green function is lost. The sweet-spot is here at  $T = 3000$ . Black circles marks the position of (the point before) the first negative  $G$ , and is an estimate of the size of the numerical noise.

We can study of the effects of varying  $T$  and  $N$  on  $G^B(t)$ .

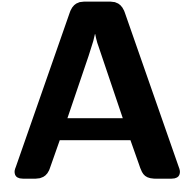
In Figure 8 we show an example for  $\kappa = 0.3$ ,  $\beta = 10$ , and  $J = 10$ . We fix the number of discretization points to  $N = 2^{19}$  and plot  $G^B(t)$  for several values of  $T$ . We have cut off the plot at the first negative value of  $G^B$ . In the plot, we observe two qualitative effects of changing  $T$ : First, upon increasing  $T$ , we find that the decay time (slope) of the Green function increases (decreases). Thus, increasing  $T$ , we allow  $G^B(t)$  to behave as if the time axis was really semi-infinite. One can perform a  $1/T$  analysis and finds that the lines have a well-defined slope in the  $T \rightarrow \infty$  limit.

Secondly, which is more subtle, we see that making  $T$  too large decreases the quality of the approximation for  $G^B(t)$ , with the optimal number being around  $T = 3000$ . We arrive at this number by the following argument: In the plot, we only show  $G^B(t)$  until the first non-negative value (at time  $t_C$ ). The solid-looking wedge shape that appears just before the first negative number is the effect of numerical oscillations that (as  $G$  decreases) become relatively more important. From the height where the “wedges” disappear (black circles connected with an orange line), we can approximate the size of this numerical error. By inspection, we see that the smallest numerical errors (and also the largest  $t_C$ ) happen for  $T = 3000$ . We can understand the loss by noting that as  $T$  grows, then (for fixed  $N$ )  $\Delta t$  also grows. In the inset of the figure, one can see

that at  $T = 30000$ ,  $\Delta t$  is so large that it even affects the continuity of the curve  $G^B(t)$ .

Choosing the appropriate  $T$ , is thus affected by the range of the Green function decay, which in turn is affected by  $\kappa$ , the ratio between the two species. In the numerics that we present in the main text, we worked with a fixed  $N$  and  $T$ , which are good when  $\kappa \approx 1$  but not when  $\kappa$  is increasingly asymmetric. Errors in the two-point function will propagate and influence the calculations of the Lyapunov exponent and explain why we see the downturn of  $\lambda$  at a characteristic value of  $\kappa$ .





# Kondo effect in Twisted Bilayer graphene

## Attribution

This paper has been previously published as a preprint on arXiv and has been submitted to Physical Review E for publications, and it is currently under the editorial review, under the title *Replicating Higgs fields in Ising gauge theory: the registry order*, together with Koenraad Schalm and Jan Zaanen.[? ]

## Abstract

The emergence of flat bands in twisted bilayer graphene at the magic angle can be understood in terms of a vanishing Fermi velocity of the Dirac cone. This is associated with van Hove singularities approaching the Fermi energy and becoming higher-order. In the density of states this is reflected by flanking logarithmic van Hove divergences pinching off the central Dirac cone in energy space. The low-energy pseudogap of the Dirac cone away from the magic angle is replaced by a power-law divergence due to the higher-order van Hove singularity at the magic angle. This plays an important role in the exotic phenomena observed in this material, such as superconductivity and magnetism, by amplifying electronic correlation effects. Here we investigate one such correlation effect – the Kondo effect due to a magnetic impurity embedded in twisted bilayer graphene. We use the Bistritzer-MacDonald model to extract the low-energy density of states of the material as a

function of twist angle, and study the resulting quantum impurity physics using perturbative and numerical renormalization group methods. Although at zero temperature the impurity is only Kondo screened precisely at the magic angle, we find highly nontrivial behavior at finite temperatures relevant to experiment, due to the complex interplay between Dirac, van Hove, and Kondo physics.

## A.1. Introduction

The properties of two-dimensional monolayer systems are strongly modified by stacking two layers with a relative twist, the so-called moiré effect in twisted bilayer systems [40]. In particular, twisted bilayer graphene (TBG) exhibits peculiar properties at specific ‘magic’ twist angles [41–50]. One characteristic of the system at these magic angles is that the non-interacting band structure contains almost-flat bands. This leads to a dramatic enhancement of the density of states (DoS). Consequently, electronic interaction effects are boosted, favoring the appearance of magnetism and other correlated phases, for example superconductivity [48–60]. Away from the magic angle in TBG, the slightly modified Dirac cones of the single layers persist [40], giving a low-energy linear pseudogap DoS. However, pronounced van Hove singularities [61] (vHs’s) dominate the band structure at higher energies, leading to logarithmic divergences in the DoS. Experimentally, it was recently shown [62] that as the magic angle is approached, the vHs divergences in the DoS move to lower energy, pinching off the Dirac cone from either side in energy space. At the magic angle, the vHs divergences in the DoS merge, and a single higher-order vHs [45] (HO-vHs) emerges, yielding a stronger, power-law divergent DoS. This is a characteristic feature of the emergent flat bands in this system. The enhanced effect of electron correlations due to the HO-vHs in the bulk TBG material has been studied theoretically [49, 50, 52, 63] and confirmed in scanning tunnelling spectroscopy (STS) experiments [64, 65].

Detailed information on the electronic structure of new materials can also be obtained by exploiting defects or impurities as *in-situ* probes [66]. The nature of the electronic scattering from impurities in a system is strongly dependent on the band structure and DoS of the clean host material, and can be probed either locally at the impurity site by STS [67, 68], or by collecting momentum-space information through quasiparticle interference (QPI) measurements [69]. For quantum impurities such as magnetic adatoms [70, 71] or single-molecule magnets [72], the impurity spin degree of freedom generates additional spin-flip scattering, which is boosted at low temperatures by the Kondo effect in standard metallic hosts [73]. The Kondo effect itself depends sensitively on the local spin-resolved DoS of the host material, and hence such ‘Kondo probes’ can provide additional electronic structure information [74] or be utilized for quantum metrology [75]. Aside from the spectroscopic and



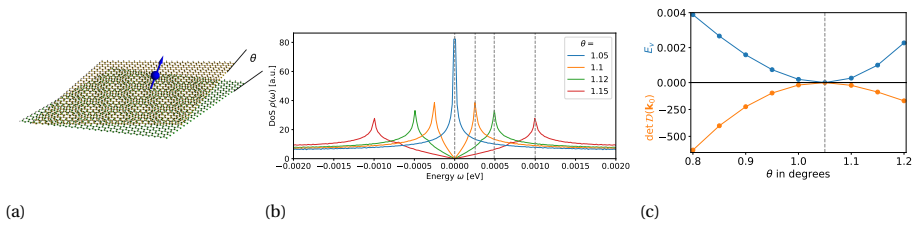


Figure A.1: (a) Schematic representation of a magnetic impurity on the surface of the twisted bilayer graphene host material, with inter-layer twist angle  $\theta$ . (b) Evolution of the clean TBG density of states for different twist angles near the magic angle at  $\theta = 1.05^\circ$ . Vertical dashed lines indicate the energy of the dispersion saddle points  $E_v$ , which determine the van Hove singularity locations. (c) Vanishing vHs saddle point scale  $E_v$  (top) and determinant of the saddle point Hessian (bottom) as the magic angle is approached, showing how two vHs's coalesce into a single HO-vHs.

QPI signatures of Kondo physics in metals [71], the Kondo effect has been studied in a range of other unconventional materials, including monolayer graphene [76–79], topological insulators [80], Dirac and Weyl semimetals [81], ferromagnets [82, 83], superconductors [84, 85], and spin liquids [86–88] – each giving its own distinctive response. In particular, for Dirac systems with a low-energy pseudogap, the depleted conduction electron DoS is known to suppress the Kondo effect [78, 80, 81] (although it can be revived upon doping [89]).

By contrast, in the case of TBG, one might expect Kondo correlations to be strongly enhanced by the flat bands and diverging DoS close to the magic angle. The study of Kondo physics in TBG, and how it evolves with twist angle, is the topic of this article. We find that magnetic impurities are sensitive probes of the nontrivial band structure of the material, and we uncover rich thermodynamic and spectroscopic signatures that rapidly change on approaching the magic angle.

Specifically, we consider a single, interacting Anderson impurity embedded in the TBG host – see Fig. A.1a. The clean TBG material is modelled using the Bistritzer-MacDonald (BM) model [42], which we discuss in Sec. A.2. We focus on the role of the vHs's and their evolution with twist angle. The model shows an intricate interplay between different DoS elements: metallic, Dirac pseudogap, vHs log-divergence, and HO-vHs power-law divergence. In Sec. A.3 we review the physics of the Kondo model, emphasizing the different limiting behaviors arising in the metallic, pseudogap, and log-diverging or power-law diverging DoS needed to understand the compound DoS structure in TBG. Finally, in Sec. A.4 we present full numerical renormalization group (NRG) results for an Anderson impurity in TBG in the vicinity of, and at, the magic angle. We focus on thermodynamic quantities such as the impurity entropy as a clear means of identifying the different fixed points and emergent energy scales. We

## A

furthermore study the energy-dependence of the local impurity spectral function, which is relevant to STS experiments. We conclude in Sec. A.5, commenting on the suitability of magnetic impurities as *in-situ* probes for the physics of TBG near the magic angle, and an outlook for experiments. Technical material is given for reference in the Appendices.

We note that the Kondo model we consider in this work is completely different from recent studies of TBG as a heavy fermion problem [90–93], where the quenched kinetic energy of the flat band lends itself to being treated as an immobile lattice of impurities. In those works, the correlated local moments are a part of the TBG lattice itself, whereas here we consider additional adatom impurities coupled to the TBG host. The effective impurity models and corresponding electronic hybridization functions are rather different in these two cases.

## A.2. Van Hove singularities in the Bistritzer-MacDonald model

Before considering a Kondo impurity in TBG, we first analyze the clean host material, focusing on how the vHs's affect the band structure and local DoS. In the first part of this section we briefly recall the details of the Bistritzer-MacDonald (BM) model of TBG and its particle-hole symmetric limit. The original derivations were performed in Refs. [41, 42, 94]; further details are provided in the Appendices. In the second part, we analyze the formation of flat bands from saddle points and discuss the detailed structure of the lowest energy bands.

### A.2.1. Particle-hole symmetric Bistritzer-MacDonald model

To describe TBG with a small twist angle  $\theta$ , it is necessary to take into account both the intralayer hopping parameter  $t$  for each of the individual graphene layers, as well as the interlayer tunneling  $w$ . In the following we take these to be  $t \approx 2.87$  eV and  $w \approx 0.11$  eV, as used in Ref. [42]. The twist angle between the layers generates a Moiré pattern with an emergent superlattice structure. For small twist angles  $\theta$ , the characteristic Moiré length scale  $L_\theta$  is given by  $L_\theta = \sqrt{3}a/[2\sin(\theta/2)]$  with  $a = 1.42\text{\AA}$  being the interatomic distance in monolayer graphene. The corresponding effective low-energy Hamiltonian near the  $K$  point of the Moiré Brillouin zone (MBZ) has the form

[42, 94],

$$H(\mathbf{k}) = \begin{pmatrix} h_{\frac{\theta}{2}}^K(\mathbf{k}) & wT_1 & wT_2 & wT_3 \\ wT_1^\dagger & h_{-\frac{\theta}{2}}^K(\mathbf{k} - \mathbf{q}_1) & 0 & 0 \\ wT_2^\dagger & 0 & h_{-\frac{\theta}{2}}^K(\mathbf{k} - \mathbf{q}_2) & 0 \\ wT_3^\dagger & 0 & 0 & h_{-\frac{\theta}{2}}^K(\mathbf{k} - \mathbf{q}_3) \end{pmatrix}. \quad (\text{A.1})$$

The wave vector  $\mathbf{k}$  is measured relative to the  $K$  point, and the Hamiltonian acts on 8-component wavefunctions  $\Psi = (\psi_{0,\mathbf{k}}, \psi_{1,\mathbf{k}}, \psi_{2,\mathbf{k}}, \psi_{3,\mathbf{k}})^T$ , where  $\psi_{0,\mathbf{k}}$  is a two-component spinor in the A-B sublattice basis in the top layer, and  $\psi_{1(2,3),\mathbf{k}}$  are spinors in bottom layer at wave vectors  $\mathbf{k} - \mathbf{q}_{1(2,3)}$ . Here  $h_{\frac{\theta}{2}}^K(\mathbf{k})$  is the effective low-energy Hamiltonian of single layer graphene near the  $K$  point, in a coordinate frame rotated by angle  $\phi$ ,

$$h_{\frac{\theta}{2}}^K(\mathbf{k}) = kv_F \begin{bmatrix} 0 & e^{i(\theta_k - \phi)} \\ e^{-i(\theta_k - \phi)} & 0 \end{bmatrix}. \quad (\text{A.2})$$

Here, the angle  $\theta_k$  measures the orientation of the momentum relative to the  $x$ -axis,  $k = |\mathbf{k}|$ , and the Fermi velocity is  $v_F = 9.3 \times 10^7$  cm/s. The wave vectors  $\mathbf{q}_{1,2,3}$  connecting  $K$ -points of the top and bottom layers are,

$$\mathbf{q}_1 = k_\theta \{0, -1\}, \quad (\text{A.3a})$$

$$\mathbf{q}_2 = k_\theta \left\{ \frac{\sqrt{3}}{2}, \frac{1}{2} \right\}, \quad (\text{A.3b})$$

$$\mathbf{q}_3 = k_\theta \left\{ -\frac{\sqrt{3}}{2}, \frac{1}{2} \right\}, \quad (\text{A.3c})$$

with Moiré wave number,  $k_\theta \equiv |\mathbf{q}_j| = \frac{8\pi}{3\sqrt{3}a} \sin\left(\frac{\theta}{2}\right)$ .

Finally, the interlayer tunneling matrices  $T_{1(2,3)}$  are expressed in terms of Pauli matrices, viz:

$$T_1 = 1 + \sigma_x, \quad (\text{A.4a})$$

$$T_2 = 1 - \frac{\sigma_x}{2} - \frac{\sqrt{3}\sigma_y}{2}, \quad (\text{A.4b})$$

$$T_3 = 1 - \frac{\sigma_x}{2} + \frac{\sqrt{3}\sigma_y}{2}. \quad (\text{A.4c})$$

The Hamiltonian Eq. (A.1) captures the essential physics of TBG and correctly predicts the first magic angle at  $\theta \simeq 1.05^\circ$ . At the  $K$  point of the MBZ one finds that the

A

lowest energy bands have a Dirac cone dispersion with an effective Fermi velocity,

$$v_F^* = \frac{1 - 3w^2 / (\hbar v_F k_\theta)^2}{1 + 6w^2 / (\hbar v_F k_\theta)^2} \quad (\text{A.5})$$

which vanishes exactly at the magic angle, where  $\hbar v_F k_\theta = \sqrt{3}w$ .

In the following, we will use the particle-hole symmetric version of the BM model. This form is obtained from Eq. (A.1) by eliminating subleading (second-order) corrections in the diagonal elements coming from the effect of the twist on the single layer Hamiltonian [94]. This is simply achieved by setting  $\phi = 0$  in Eq. (A.2),

$$H(\mathbf{k}) = \begin{pmatrix} h_0^K(\mathbf{k}) & wT_1 & wT_2 & wT_3 \\ wT_1^\dagger & h_0^K(\mathbf{k} - \mathbf{q}_1) & 0 & 0 \\ wT_2^\dagger & 0 & h_0^K(\mathbf{k} - \mathbf{q}_2) & 0 \\ wT_3^\dagger & 0 & 0 & h_0^K(\mathbf{k} - \mathbf{q}_3) \end{pmatrix}. \quad (\text{A.6})$$

The low-energy TBG DoS  $\rho(\omega)$ , obtained by diagonalizing this Hamiltonian is shown in Fig. A.1b, for different twist angles in the vicinity of the magic angle at  $\theta = 1.05^\circ$ . When precisely at the magic angle, we see a single divergence in the DoS at the Fermi energy. We measure energies relative to the Fermi energy and set  $E_F = 0$ , such that  $\rho(\omega) = \rho(-\omega)$ , embodying the particle-hole symmetry of Eq. (A.6). However, moving away from the magic angle, we have a Dirac cone feature, with pseudogap vanishing DoS  $\rho(\omega) \sim |\omega|$  below an emergent scale  $|\omega| \ll E_v$ . We also see two vHs points with diverging DoS at  $\omega = \pm E_v$ . Below we analyze the low-energy bands and vHs structure of the model, extracting the angle dependence of the vHs scale  $E_v$ .

### A.2.2. Characterization of van Hove singularities in the particle-hole symmetric BM model

We start our analysis of vHs properties in TBG by recalling the classification recently introduced in Refs. [45, 95, 96], which expands the definition from the usual vHs with logarithmically diverging DoS [61] to include HO-vHs with power-law diverging DoS. For a band dispersion  $\epsilon(\mathbf{k})$ , which is a function of the 2D momentum vector  $\mathbf{k}$ , we calculate the first derivatives  $\nabla_{\mathbf{k}}\epsilon(\mathbf{k})$ , and the Hessian matrix of second derivatives  $\mathcal{D}_{ij}(\mathbf{k}) \equiv \frac{1}{2}\partial_{k_i}\partial_{k_j}\epsilon(\mathbf{k})$ . The Hellman-Feynman theorem allows to carry this out with high numerical accuracy (see Appendix A). A logarithmic vHs arises at a point  $\mathbf{k}_0$  in the dispersion corresponding to a saddle point when:

$$\text{log vHs: } \nabla_{\mathbf{k}}\epsilon(\mathbf{k}_0) = \mathbf{0} \quad \text{and} \quad \det \mathcal{D}(\mathbf{k}_0) < 0. \quad (\text{A.7})$$

The negative Hessian determinant means that we have both a maximum and a minimum in each of the principal directions of the saddle point. A higher-order saddle

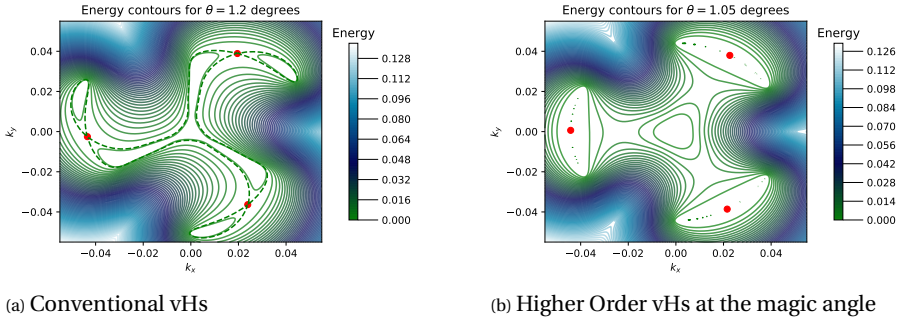


Figure A.2: Low-energy features of the particle-hole symmetric BM model of pristine TBG, showing energy contours of the dispersion  $\epsilon(\mathbf{k})$  as a function of momentum  $\mathbf{k}$  in the extended MBZ. Red points show the saddle points of the dispersion, corresponding to the van Hove singularities. Dashed lines show the contours at energy  $E_v$ , on which the van Hove points sit.

point, corresponding to a HO-vHs, is instead characterized by zero determinant of Hessian matrix:

$$\text{HO-vHs: } \nabla_{\mathbf{k}}\epsilon(\mathbf{k}_0) = \mathbf{0} \text{ and } \det \mathcal{D}(\mathbf{k}_0) = 0. \quad (\text{A.8})$$

In addition, higher-order saddle points can be classified according to the leading polynomial terms in an expansion of the dispersion  $\epsilon(\mathbf{k})$  around the saddle point  $\mathbf{k}_0$  [95, 96]. These leading terms in the expansion correspond directly to the numerical exponent of the power-law divergence in the DoS.

With the help of this classification, we proceed to investigate the structure of the lowest band in the BM model Hamiltonian given by Eq. (A.6). Using particle-hole symmetry in conjunction with the transformation  $k_x \rightarrow -k_x$  allows us to concentrate only on the lowest positive energy band for our analysis. Technical details of our numerical implementation are presented in Appendix A. In Fig. A.1c we show the numerically-computed  $E_v$  scale (top panel) and the determinant of the saddle-point Hessian  $\det \mathcal{D}(\mathbf{k}_0)$  (bottom panel) as a function of twist angle. Both are seen to vanish at the magic angle, heralding the emergence of the HO-vHs at this point. This behavior is further analyzed below.

In Fig. A.2 we plot the momentum-resolved spectrum of the BM model for twist angles  $\theta = 1.2^\circ$  (panel a) and  $\theta = 1.05^\circ$  (panel b). We compute  $\nabla_{\mathbf{k}}\epsilon(\mathbf{k})$  throughout the MBZ and search for the vHs points for which  $\nabla_{\mathbf{k}}\epsilon(\mathbf{k}) = \mathbf{0}$ . These are indicated in both panels as the red circle points.

Having located the vHs points in the MBZ for a given twist angle, we can classify them and study their neighborhood in momentum space. Away from the magic angle (e.g. for  $\theta = 1.2^\circ$  shown in Fig. A.2a), we indeed find a negative determinant of the Hessian  $\det \mathcal{D}(\mathbf{k}_0) < 0$ , and the vHs's have a local hyperbolic geometry in momentum

A

space. The dispersion is found to have the leading form,

$$\epsilon_{\mathbf{p}} = E_v + \alpha p_x^2 - \beta p_y^2, \quad (\text{A.9})$$

where the coefficients are obtained from the eigenvalues of the Hessian, and the labels  $p_x$  and  $p_y$  are measured in the principal directions of the saddle point, with  $\mathbf{p} = 0$  defining the saddle point itself. The corresponding leading correction to the DoS then takes the form,

$$\rho(\omega) = \frac{1}{4\pi^2} \frac{1}{\sqrt{\alpha\beta}} \ln \left| \frac{D}{\omega - E_v} \right|, \quad (\text{A.10})$$

where  $D$  is a high-energy cutoff, taken to be the conduction electron bandwidth. In this way, we may extract the vHs scale  $E_v$ .

As we begin twisting toward the magic angle, the vHs energy scale  $E_v$  starts to decrease, and the two logarithmic singularities at  $\omega = \pm E_v$  therefore move closer together. Furthermore, the magnitude of the Hessian at the vHs,  $|\det \mathcal{D}(\mathbf{k}_0)|$ , also decreases. The two vHs points merge at  $\omega = 0$  precisely at the magic angle  $\theta = 1.05^\circ$  [62], at which point the Hessian also vanishes,  $\det \mathcal{D}(\mathbf{k}_0) = 0$ . This transition is shown in Fig. A.1c. As the magic angle is approached and the HO-vHs is formed, we see a further flattening of the dispersion in the  $p_y$  direction. The fittingly-named higher-order singularity requires a higher-order polynomial to faithfully capture its dispersion. The lowest polynomial which correctly captures all the symmetries is given by,

$$\epsilon_{\mathbf{p}} = \alpha p_x^2 + \gamma p_x p_y^2 + \kappa p_y^4. \quad (\text{A.11})$$

This comes hand-in-hand with a sharper, power-law divergence in the DoS,

$$\rho(\omega) = (2\pi)^{-\frac{5}{2}} \Gamma(\frac{1}{4})^2 (4\alpha\tilde{\Gamma}^2)^{-1/4} |\omega|^{-1/4}, \quad (\text{A.12})$$

with  $\tilde{\Gamma}^2 = \gamma^2 - 4\alpha\kappa$  and  $\Gamma(x)$  the usual gamma function.

The low-energy DoS at different angles can be computed numerically by binning histograms of energies for the lowest band of the BM model, as shown in Fig. A.1b. Away from the magic angle, the numerical calculation indicates a linear DoS around the Fermi energy, coming from the Dirac cone in the spectrum. Around  $\omega = \pm E_v$  we see the vHs log-divergences. At the magic angle, the HO-vHs around the Fermi energy ‘eat up’ the Dirac cone, and we have instead a large DoS at low energies, diverging as  $\rho(\omega) \sim |\omega|^{-1/4}$ .

### A.3. The Kondo problem

The Kondo effect is a classic paradigm in many-body quantum physics [73]. The corresponding Kondo model features a single quantum spin- $\frac{1}{2}$  magnetic impurity cou-

pled by antiferromagnetic exchange to a single channel of non-interacting conduction electrons. Originally, the Kondo model was formulated to describe dilute magnetic impurities such as iron, in bulk metals such as gold [70, 97]. In these metallic systems, an impurity local moment becomes strongly entangled with its surrounding conduction electrons at low temperatures, and is dynamically screened [98–100]. This leads to dramatically enhanced spin-flip scattering in the host metal, which can be detected spectroscopically [71].

A more microscopic starting point is provided by the single impurity Anderson model [73], which describes the impurity as a single quantum orbital with strong electron interactions,

$$H_{\text{AM}} = H_{\text{host}} + \epsilon_d \sum_{\sigma} d_{\sigma}^{\dagger} d_{\sigma} + U_d d_{\uparrow}^{\dagger} d_{\uparrow} d_{\downarrow}^{\dagger} d_{\downarrow} + g \sum_{\sigma} \left( d_{\sigma}^{\dagger} c_{0,\sigma} + c_{0,\sigma}^{\dagger} d_{\sigma} \right), \quad (\text{A.13})$$

where  $d_{\sigma}^{(\dagger)}$  is an annihilation (creation) operator for an impurity electron with spin  $\sigma = \uparrow/\downarrow$ , and  $H_{\text{host}} = \sum_{k,\sigma} \epsilon_k c_{k,\sigma}^{\dagger} c_{k,\sigma}$  describes the clean host. Here  $c_{k,\sigma}^{(\dagger)}$  annihilates (creates) a conduction electron of the host material with momentum  $k$  and spin  $\sigma$ . We do not employ band indices in this expression. The impurity couples locally in real-space to the effective host orbital  $c_{0,\sigma} = \sum_k \xi_k c_{k,\sigma}$ , where  $\xi_k$  is the weight of state  $k$  at the impurity location (taken to be at the origin).

For small host-impurity hybridization  $g$ , repulsive Coulomb interaction  $U_d > 0$ , and suitably-chosen impurity potential  $-\epsilon_d < \epsilon_d < 0$ , a spin- $\frac{1}{2}$  local moment can be trapped on the impurity. Projecting onto this doubly-degenerate spin- $\frac{1}{2}$  manifold of impurity states by eliminating virtual excitations to empty or doubly-occupied impurity configurations by means of a Schrieffer-Wolff (SW) transformation [73, 101] yields the simpler Kondo model,

$$H_{\text{KM}} = H_{\text{host}} + J \mathbf{S} \cdot \mathbf{s}_0 + V \sum_{\sigma} c_{0,\sigma}^{\dagger} c_{0,\sigma}, \quad (\text{A.14})$$

where  $J > 0$  is the antiferromagnetic exchange interaction between the impurity spin- $\frac{1}{2}$  degree of freedom  $\mathbf{S}$ , and the *spin density* of the host conduction electrons at the impurity position  $\mathbf{s}_0 = \frac{1}{2} \sum_{\alpha,\beta} c_{0,\alpha}^{\dagger} \boldsymbol{\sigma}_{\alpha\beta} c_{0,\beta}$ , where  $\boldsymbol{\sigma}$  is the vector of Pauli matrices. The third term describes potential scattering of the host conduction electrons induced by the impurity (since  $c_{0,\sigma}^{\dagger} c_{0,\sigma} = \sum_{k,k'} \xi_k \xi_{k'} c_{k,\sigma}^{\dagger} c_{k',\sigma}$ ).

The standard Schrieffer-Wolff result [73, 101], which becomes exact in the limit  $U_d/g^2 \rightarrow \infty$ , yields  $J = 2g^2[(U_d + \epsilon_d)^{-1} - (\epsilon_d)^{-1}]$  and  $V = -g^2[(U_d + \epsilon_d)^{-1} + (\epsilon_d)^{-1}]$ . At the particle-hole symmetric point of the model  $\epsilon_d = -U_d/2$ , we therefore obtain  $J = 8g^2/U_d$  and  $V = 0$  (the latter result can be viewed as a many-body quantum destructive interference effect between particle and hole processes). Although the Kondo model Eq. (A.14) correctly captures the low-energy physics of Eq. (A.13), it

A

should be noted that for realistic values of  $U_d$ ,  $\epsilon_d$ , and  $g$  outside of the strict perturbative regime, the values of the effective parameters  $J$  and  $V$  must be obtained by more sophisticated means that take into account renormalization from the conduction electrons and the specific conduction electron DoS [102]. We also emphasize that  $J$  and  $V$  are not independent parameters in Eq. (A.14), being both derived from the same microscopic parameters of the underlying Anderson model.

The physics of the impurity problem is controlled by the local (free) conduction electron DoS seen by the impurity,  $\rho_\sigma(\omega) = -\frac{1}{\pi} \text{Im} \langle\langle c_{0,\sigma}; c_{0,\sigma}^\dagger \rangle\rangle^0$ , where  $\langle\langle c_{0,\sigma}; c_{0,\sigma}^\dagger \rangle\rangle$  is the retarded, real-frequency local host Green's function at the impurity position, and the 0 superscript denotes that it is calculated for the clean host.

In this work we consider a single magnetic impurity (the ‘dilute limit’) embedded in an otherwise clean host TBG system modelled by the BM model.  $SU(2)$  spin symmetry is taken to be unbroken. We also assume that the impurity couples equally to all BM bands independently of the impurity position ( $\xi_k$  is constant for all momenta and band indices), such that  $\rho_\sigma(\omega) \equiv \rho(\omega)$  is the TBG DoS, whose low-energy form is described by Eqs. (A.10) or (A.12). This is certainly a simplification, since details of the impurity-TBG hybridization will naturally affect details of the impurity response. The specific form of the impurity hybridization function will in practice depend on the impurity location within the moiré unit cell and how the impurity couples in real-space to the constituent TBG carbon atoms. We leave such *ab initio* studies for future work. However, the rich physics uncovered below will remain qualitatively unaltered provided the impurity hybridization function still features van Hove divergences flanking a central pseudogap Dirac cone. Since the origin of these features is rooted deeply in the symmetry and topology of the TBG material, we expect the idealized Kondo physics described here to be rather generic. On the other hand, insights from monolayer graphene [79] indicate that the physics of vacancies in TBG or substitutional dopants may drastically differ, since the local DoS in these cases is strongly modified.

In the rest of this section we review the methods that we use to attack the problem as well as the quantities to be analyzed.

### A.3.1. Poor man’s scaling approach

The Kondo model as defined by Eq. (A.14) is a nontrivial strong correlation problem. For metallic host systems, the first insights were provided by Kondo’s calculation of the scattering T-matrix [97], which is related to the impurity spectral function. Kondo found a low-temperature divergence in perturbation theory: even when the bare  $J$  is small, straight perturbation theory does not give a good description of the low-temperature physics or a proper understanding of the many-body ground state of



the system. This divergence was better understood by Anderson's self-coined 'poor-man's scaling' approach [103] – a precursor to the renormalization group (RG). It identified an emergent low-energy scale  $T_K$  – the Kondo temperature – below which perturbation theory breaks down, and the problem becomes a strong coupling problem. We briefly introduce the method here, since we will employ it in the next section to understand analytically the scaling properties of an impurity in the TBG host.

Conventionally in the poor man's scaling approach, one uses dimensionless couplings  $j = \rho_0 J$  and  $v = \rho_0 V$  with  $\rho_0 = \rho(\omega = 0)$  the Fermi level DoS. However, for consideration of Dirac systems where  $\rho_0$  may in fact vanish, a different choice is required. Here we simply use the original dimensionful couplings  $J$  and  $V$ . Furthermore, we assume that the host DoS is particle-hole symmetric, meaning  $\rho(\omega) = \rho(-\omega)$ , a property satisfied by Eq. (A.6); and is defined within a band of halfwidth  $D$ , meaning  $\rho(\omega) \propto \theta(D - |\omega|)$ .

Anderson's scaling procedure goes as follows [103]: (i) integrate out high energy conduction electron states  $D - \delta D < |\omega| < D$  close to the band edges in a shell of width  $\delta D$ ; (ii) incorporate the effect of virtual excitations to these eliminated states perturbatively by rescaling the couplings  $J$  and  $V$  to give an effective Hamiltonian of the same form but defined with a reduced bandwidth  $D \rightarrow D - \delta D$ ; (iii) study the flow of the parameters  $J$  and  $V$  on successive reduction of the bandwidth. Making  $\delta D$  infinitesimal, one obtains the following scaling equations,

$$\begin{aligned} \frac{dJ}{dD} &= -\frac{\rho(D)}{D} J^2, \\ \frac{dV}{dD} &= 0. \end{aligned} \tag{A.15}$$

The first equation determines the flow of the coupling constant  $J$  on reducing the bandwidth, whereas the second equation shows that the potential scattering  $V$  does not flow. If the bare model is particle-hole symmetric then no potential scattering is generated under the scaling procedure. In the remainder of this paper we will focus on the case  $V = 0$ . The scaling equation for  $J$  gives insight into the breakdown of perturbation theory and hence  $T_K$ , by identifying the point where the rescaled  $J$  diverges. We consider various relevant situations in the following.

### A.3.2. Numerical Renormalization Group

Wilson's numerical renormalization group [104, 105] (NRG) is a non-perturbative technique for solving quantum impurity type problems. It builds upon Anderson's perturbative scaling ideas [103], but overcomes its limitations by establishing a more general framework in terms of which physical quantities can be calculated numerically-exactly, down to zero temperature. Wilson's original formulation of NRG [104], designed to obtain the thermodynamic properties of a single magnetic

A

impurity in a metal, has since been extended to deal with arbitrary host systems [105, 106], and to the calculation of dynamical quantities via the full-density-matrix NRG approach [107, 108]. The former has allowed NRG to be applied to monolayer graphene [77], and other Dirac systems [80, 81]. The latter provides access to highly accurate spectral data, with excellent real-frequency resolution, at any temperature. NRG has also been adapted over the years to extend the range of problems that can be tackled and improve accuracy or efficiency [109–115], making it the gold-standard method of choice for solving generalized quantum impurity problems.

The basic NRG algorithm [104, 105] proceeds as follows. (i) The local conduction electron density of states  $\rho(\omega)$  of the pristine host material (without the impurity) must first be calculated.

(ii) This DoS is then discretized logarithmically by dividing it up into intervals according to the discretization points  $\pm D\Lambda^{-n}$ , where  $D$  is the bare conduction electron bandwidth,  $\Lambda > 1$  is the NRG discretization parameter, and  $n = 0, 1, 2, 3, \dots$ . The continuous electronic density in each interval is replaced by a single pole at the average position with the same total weight, yielding  $\rho^{\text{disc}}(\omega)$ .

(iii) The conduction electron part of the Hamiltonian  $H_{\text{host}}$  is then mapped into the form of a ‘Wilson chain’,

$$H_{\text{host}} \rightarrow H_{\text{host}}^{\text{disc}} = \sum_{\sigma} \sum_{n=0}^{\infty} \left[ t_n \left( f_{n,\sigma}^{\dagger} f_{n+1,\sigma} + f_{n+1,\sigma}^{\dagger} f_{n,\sigma} \right) + \epsilon_n f_{n,\sigma}^{\dagger} f_{n,\sigma} \right], \quad (\text{A.16})$$

where the Wilson chain coefficients  $\{t_n\}$  and  $\{\epsilon_n\}$  are determined such that the DoS at the end of the chain reproduces exactly the discretized host DoS, that is  $-\frac{1}{\pi} \text{Im} \langle \langle f_{0,\sigma}; f_{0,\sigma}^{\dagger} \rangle \rangle = \rho^{\text{disc}}(\omega)$ . For a system with particle-hole symmetry,  $\epsilon_n = 0$  for all  $n$ . Due to the logarithmic discretization, the Wilson chain hopping parameters decay roughly exponentially down the chain,  $t_n \sim \Lambda^{-n/2}$ , although the precise details are also important since they encode the specific host DoS [105].

(iv) The impurity is coupled to site  $n = 0$  of the Wilson chain. We define a sequence of Hamiltonians  $H_N$  comprising the impurity and the first  $N$  Wilson chain sites,

$$H_N = H_{\text{imp}} + H_{\text{hyb}} + \sum_{\sigma} \left[ \sum_{n=0}^N \epsilon_n f_{n,\sigma}^{\dagger} f_{n,\sigma} + \sum_{n=0}^{N-1} t_n \left( f_{n,\sigma}^{\dagger} f_{n+1,\sigma} + f_{n+1,\sigma}^{\dagger} f_{n,\sigma} \right) \right], \quad (\text{A.17})$$

where for the Anderson model  $H_{\text{imp}} = \epsilon_d \sum_{\sigma} d_{\sigma}^{\dagger} d_{\sigma} + U_d d_{\uparrow}^{\dagger} d_{\uparrow} d_{\downarrow}^{\dagger} d_{\downarrow}$  and  $H_{\text{hyb}} = g \sum_{\sigma} (d_{\sigma}^{\dagger} f_{0,\sigma} + f_{0,\sigma}^{\dagger} d_{\sigma})$  while for the Kondo model  $H_{\text{imp}} + H_{\text{hyb}} = J \mathbf{S} \cdot \mathbf{s}_0 + V \sum_{\sigma} f_{0,\sigma}^{\dagger} f_{0,\sigma}$

with  $\mathbf{s}_0 = \frac{1}{2} \sum_{\alpha, \beta} f_{0, \alpha}^\dagger \boldsymbol{\sigma}_{\alpha \beta} f_{0, \beta}$ . From Eq. (A.17) we obtain the recursion relation,

$$H_N = H_{N-1} + \sum_{\sigma} \left[ \epsilon_N f_{N, \sigma}^\dagger f_{N, \sigma} + t_N \left( f_{N-1, \sigma}^\dagger f_{N, \sigma} + f_{N, \sigma}^\dagger f_{N-1, \sigma} \right) \right], \quad (\text{A.18})$$

such that the full (discretized) model is obtained as  $H^{\text{disc}} = \lim_{N \rightarrow \infty} H_N$  [116].

(v) Starting from the impurity, we build up the chain by successively adding Wilson chain sites using the recursion, Eq. (A.18). At each step  $N$ , the intermediate Hamiltonian  $H_N$  is diagonalized, and only the lowest  $N_s$  states are retained to construct the Hamiltonian  $H_{N+1}$  at the next step (the higher energy states are discarded). In such a way, we focus on progressively lower energy scales with each iteration. Furthermore, the iterative diagonalization and truncation procedure can be viewed as an RG transformation [104],  $H_{N+1} = \mathcal{R}[H_N]$ .

(vi) The partition function  $Z_N$  can be calculated from the diagonalized Hamiltonian  $H_N$  at each step  $N$ . Wilson used RG arguments to show [104] that thermodynamic properties obtained from  $Z_N$  at an effective temperature  $T_N \sim \Lambda^{-N/2}$  accurately approximate those of the original undiscretized model at the same temperature. The sequence of  $H_N$  can therefore be viewed as coarse-grained versions of the full model, which faithfully capture the physics at progressively lower and lower temperatures.

(vii) The discarded states at each step form a complete set (the Anders-Schiller basis [107]), from which the NRG full density matrix can be constructed. This provides a rigorous way of calculating real-frequency dynamical quantities via the Lehmann representation [108].

In this work, we take the DoS  $\rho(\omega)$  of the TBG system for a given twist angle  $\theta$  (as calculated from the BM model in Sec. A.2), discretize it logarithmically, and map to Wilson chains. The DoS used and the resulting Wilson chains are shown in Appendix B. NRG is then used to solve the Anderson and Kondo models describing an impurity embedded in the TBG host. Thermodynamic and dynamical quantities are calculated and discussed in Sec. A.4. Throughout, we use an NRG discretization parameter  $\Lambda = 2$  and retain  $N_s = 4000$  states at each step of the calculation.

### A.3.3. Observables

The physics of an impurity in the TBG host can be characterized by a number of observables, both thermodynamic and dynamical. Here we consider the impurity contribution to the total thermal entropy  $S_{\text{imp}}(T)$  as a function of the temperature  $T$ , and the low- $T$  impurity spectral function  $A(\omega)$  as a function of energy  $\omega$ .

The impurity entropy readily allows us to extract the Kondo scale  $T_K$  from NRG data, to track accurately the RG flow, and to identify RG fixed points. It is defined as  $S_{\text{imp}}(T) = S_{\text{tot}}(T) - S_0(T)$ , where  $S_{\text{tot}}$  is the entropy of the entire system, while  $S_0$  is

A

the entropy of the free TBG host without impurities. The residual impurity entropy  $S_{\text{imp}}(T = 0)$ , is a finite universal number of order unity which characterizes the stable RG fixed point and hence the ground state of the system; for example  $S_{\text{imp}}(0) = \ln 2$  for a free, unscreened impurity spin  $S = \frac{1}{2}$  local moment.

The impurity spectral function gives dynamical information and is accessible experimentally via scanning tunneling spectroscopy (STS), which probes the energy-resolved impurity density of states [71]. For an Anderson impurity it is related to the impurity Green's function,  $A(\omega) = -\frac{1}{\pi} \text{Im } G_{dd}(\omega)$  where  $G_{dd}(\omega) = \langle\langle d_\sigma; d_\sigma^\dagger \rangle\rangle$ .

Electronic scattering in the TBG system induced by the impurity is characterized by the t-matrix, which in turn is controlled by the impurity Green's function. In momentum space, the t-matrix equation reads,

$$G_{kk'}(\omega) = \delta_{kk'} G_{kk}^0(\omega) + G_{kk}^0(\omega) T_{kk'}(\omega) G_{k'k'}^0(\omega), \quad (\text{A.19})$$

where  $G_{kk'}^{(0)}(\omega) = \langle\langle c_{k,\sigma}; c_{k',\sigma}^\dagger \rangle\rangle^{(0)}$  is the electron Green's function for the full (free) TBG system with (without) the impurity, and  $T_{kk'}(\omega) = g^2 \xi_k \xi_{k'} G_{dd}(\omega)$  is the t-matrix itself. Transforming to real space, the t-matrix equation becomes,

$$G_{\mathbf{r}_i \mathbf{r}_j}(\omega) = G_{\mathbf{r}_i \mathbf{r}_j}^0(\omega) + G_{\mathbf{r}_i \mathbf{r}_0}^0(\omega) T(\omega) G_{\mathbf{r}_0 \mathbf{r}_j}^0(\omega), \quad (\text{A.20})$$

where  $G_{\mathbf{r}_i \mathbf{r}_j}^{(0)}(\omega)$  are the full (free) electronic propagators between real-space sites  $\mathbf{r}_i$  and  $\mathbf{r}_j$  of the TBG system, and the local t-matrix is  $T(\omega) = g^2 G_{dd}(\omega)$ . The impurity is taken to be located at site  $\mathbf{r}_0$ .

A related experimental quantity obtained by Fourier transform STS [69] (FT-STs) is the quasiparticle interference (QPI) pattern, defined as,

$$\Delta\rho(\mathbf{q}, \omega) = \sum_i e^{-i\mathbf{q} \cdot \mathbf{r}_i} \Delta\rho(\mathbf{r}_i, \omega), \quad (\text{A.21})$$

where  $\Delta\rho(\mathbf{r}_i, \omega) = -\frac{1}{\pi} \text{Im} [G_{\mathbf{r}_i \mathbf{r}_i}(\omega) - G_{\mathbf{r}_i \mathbf{r}_i}^0(\omega)]$  is the difference in electronic density at site  $\mathbf{r}_i$  due to the impurity. As such, the QPI pattern  $\Delta\rho(\mathbf{q}, \omega)$  can be obtained entirely from the free TBG propagators and the impurity Green's function, via the t-matrix equation.

In the following, we study the zero temperature,  $T = 0$ , impurity spectral function  $A(\omega)$  using NRG; the t-matrix and QPI can be obtained from this as described above.

### A.3.4. Limiting cases of the Kondo problem

The physics of the Kondo model strongly depends on the host DoS. For the problem of a magnetic impurity in a TBG host, as modelled using the BM model, there are a number of relevant limits. We assume that the impurity couples to all the orbitals in

	Density of States, $\rho(\omega)$	Kondo Temperature, $T_K$	Impur
Metal	$\rho_0$ : constant	$De^{-1/\rho_0 J}$	A
Standard van-Hove	$\rho_0 [1 + a \ln(D/ \omega )]$ : log diverging	$De^{\frac{1}{a} - \frac{1}{a} \sqrt{1 + \frac{2a}{\rho_0 J}}}$	
Higher Order van-Hove	$\rho_0  \omega ^{-\alpha}$ : power-law diverging	$D \left(1 + \frac{\alpha D^\alpha}{\rho_0 J}\right)^{-1/\alpha}$	
Dirac cone	$\rho_0  \omega $ : linear pseudogap	$T_K = 0$	

Table A.1: Summary of properties for the Kondo model with the different host DoS encountered in this work.

the same way meaning the local TBG DoS  $\rho(\omega)$  is the only relevant quantity characterizing the host. Furthermore, we consider here the particle-hole symmetric case  $V = 0$  for simplicity.

The main insights of the ensuing discussion are summarized in Table A.1.

### The metallic limit

The case of a magnetic impurity embedded in a metallic host is the most commonly encountered and well-studied situation, with extensive literature to its name (see Ref. [73] for an introduction). The most important feature of the problem is that upon reducing the temperature, the system becomes increasingly strongly correlated. This is captured by the poor-man's scaling equation, Eq. (A.15). In a metal, it is a reasonable assumption that the DoS is roughly constant within the relevant energy window,  $\rho(\omega) \approx \rho_0$ . Integrating Eq. (A.15) then straightforwardly yields,

$$J(\Lambda) = \frac{J_0}{1 + \rho_0 J_0 \ln\left(\frac{\Lambda}{D}\right)}, \quad (\text{A.22})$$

where  $\Lambda$  is the energy scale of interest whereas  $D$  is the starting high-energy cutoff (physically  $D$  is the conduction electron bandwidth).  $J_0$  is the starting value of the coupling constant at the scale  $D$  (with  $J_0 \equiv J$  in Eq. (A.14)) whereas  $J(\Lambda)$  is the running coupling strength at energy scale  $\Lambda$ . Perturbation theory breaks down, once the running coupling  $J(\Lambda = T_K) \rightarrow \infty$ . This happens at the root of the denominator and the corresponding running energy scale reads

$$T_K = De^{-1/(\rho_0 J_0)}. \quad (\text{A.23})$$

This energy scale has a number of interpretations. One implication is that for temperatures  $T \gg T_K$ , the physics can be captured using a perturbative expansion around  $J = 0$ , meaning the limit of a free impurity henceforth referred to as the local moment (LM) regime. Consequently, the impurity entropy, up to small correction, is that of a free spin, meaning  $S_{\text{imp}}^{\text{LM}} = \log 2$ .

## A

Conversely, for  $T \sim T_K$ , perturbation theory breaks down. Nozières showed [117] that at zero temperature, the ground state is a complicated many-body spin-singlet state and the system is a local Fermi liquid. The low-temperature limit  $T \ll T_K$  is referred to as the strong coupling (SC) regime. The corresponding impurity entropy is that of a unique state with  $S_{\text{imp}}^{\text{SC}} = 0$ . The strong coupling physics in this regime shows up in the local spectral function  $A(\omega)$  as a strong quasiparticle resonance around the Fermi energy, with a spectral pinning condition satisfying the Friedel sum rule [73]. The RG flow between the two fixed points is relatively simple, with  $J(\Lambda)$  increasing from LM to SC as the energy scale  $\Lambda$  is decreased. This is illustrated in the upper panel of Fig. A.3. The Kondo scale  $T_K$  is the scaling invariant along this RG flow. Note that in the metallic case, the potential scattering  $V$  is strictly marginal and consequently plays no role.

### Close to a van Hove singularity

This case is a twist on the usual metallic Kondo problem, with very similar physics. The poor man's scaling analysis points to an RG flow from weak to strong coupling, with the running coupling  $J(\Lambda)$  again increasing from LM to SC as the energy scale  $\Lambda$  is decreased (Fig. A.3, upper panel). The main difference from the standard metallic case is an enhanced Kondo temperature [118–120] due to the enhanced DoS, which diverges logarithmically at low energies for standard vHs points. Taking the low-energy form of the DoS to be  $\rho(\omega) = \rho_0 (1 + a \ln(D/|\omega|))$ , we can integrate Eq. (A.15) and, as before, extract the Kondo scale from the divergence in  $J(\Lambda)$ . In this case we obtain,

$$T_K = D e^{\frac{1}{a} - \frac{1}{a} \sqrt{1 + \frac{2a}{\rho_0 J_0}}} . \quad (\text{A.24})$$

Note that for  $a \rightarrow 0$  the DoS becomes metallic and we recover the metallic limit result for  $T_K$ .

This expression has two limiting cases and the relevant parameter is now  $a/(\rho_0 J_0)$ : (i) For  $a/(\rho_0 J_0) \ll 1$ , the logarithmic enhancement of the DoS plays no role and one recovers the metallic limit result,  $T_K = D e^{-1/(\rho_0 J_0)}$  since the system starts out already close to the SC fixed point; (ii) In the opposite limit,  $a/(\rho_0 J_0) \gg 1$ , we find  $T_K = D e^{-\sqrt{\frac{2}{a\rho_0 J_0}}}$ , which is strongly boosted relative to the metallic case. The Kondo temperature  $T_K$  is therefore enhanced in the vicinity of a vHs. As expected, the impurity entropy is quenched at low temperatures,  $S_{\text{imp}}(T \rightarrow 0) = 0$ , embodying Kondo singlet formation. In terms of the impurity spectral function  $A(\omega)$ , the quasiparticle Kondo resonance around the fermi energy is in fact suppressed logarithmically by the logarithmically diverging DoS of the free host [74]. However, the fact that  $A(\omega = 0) = 0$  should not in this case be interpreted as a flow towards weak coupling since the relevant quantity is rather  $\rho(\omega) \times A(\omega)$ , which remains finite as  $|\omega| \rightarrow 0$  and satisfies a generalized Friedel sum rule [121] for strong coupling physics.

### Close to a Higher Order van Hove singularity

As discussed in Sec. A.2, a HO-vHs is characterized by a power-law divergence in the DoS. In the following discussion, we neglect the metallic background on top of which the power-law divergence sits, and take the DoS to be of the form  $\rho(\omega) = \rho_0|\omega|^{-\alpha}$  with  $0 < \alpha < 1$ . This problem falls into the class of power-law Kondo problems [122]. Intuitively, one expects the Kondo temperature to be further enhanced through the more strongly divergent DoS. Integrating Eq. (A.15) with this DoS yields,

$$T_K = \frac{D}{\left(1 + \frac{\alpha D^\alpha}{\rho_0 J_0}\right)^{1/\alpha}}. \quad (\text{A.25})$$

This problem also has two limits, one characterized by the local moment physics of a free impurity (LM) the other limit by a particle-hole symmetric strong coupling fixed point that we henceforth call  $\text{SSC}_{\text{HO}}$ . This RG fixed point has properties that are slightly different from the metallic strong coupling fixed point SC. It is characterized by a  $T \rightarrow 0$  impurity entropy of  $S_{\text{imp}} = -2\alpha \ln 2$ , which is negative. We emphasize that although the total thermodynamic entropy is of course never negative, the *impurity contribution* to the total system entropy as defined in Sec. A.3.3 can be negative, if the presence of the impurity causes dramatic changes to the host (local) electronic structure, relative to the clean host. This is precisely the case for the power-law Kondo model [122]. As for the impurity spectral function, the quasiparticle Kondo resonance is suppressed by the divergent free host DoS, and we find  $A(\omega) \sim |\omega|^\alpha$  at low energies. But again, the signature of Kondo singlet formation and strong coupling physics is that  $\rho(\omega) \times A(\omega)$  remains finite as  $|\omega| \rightarrow 0$ , which is indeed the case for  $\text{SSC}_{\text{HO}}$ .

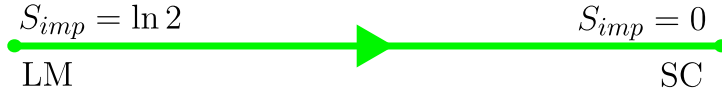
The RG flow in the particle-hole symmetric case considered here is again one-dimensional, running from LM to  $\text{SSC}_{\text{HO}}$  as the energy scale or temperature is reduced (see middle panel of Fig. A.3). We note that strong particle-hole asymmetry can play a role in the power-law Kondo model, unlike the pure metallic case, and leads to the intricate phase diagram discussed in Ref. [122].

### The limit of a two-dimensional Dirac cone

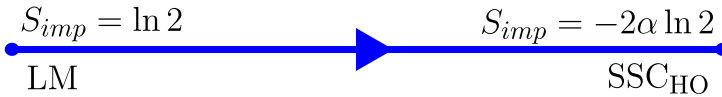
The linear vanishing DoS associated with a Dirac cone in two dimensional systems gives rise to a subtle impurity problem which falls into the class of so-called pseudogap Kondo models. This is by far the most complicated situation; it has been discussed at length in Refs. [78, 121, 123–125]. In the following, we focus on the particle-hole symmetric case, with a linear pseudogap  $\rho(\omega) = \rho_0|\omega|$  that is characteristic of 2d Dirac materials. Naively, one might expect a reduced Kondo temperature due to the reduced DoS of a Dirac cone compared with that of a metal. In fact, the Kondo effect is suppressed entirely in this case and  $T_K$  vanishes, regardless of the strength of

A

(1),(2) Metal/vHs



(3) HO-vHs



(4) Dirac



Figure A.3: One-dimensional RG diagram showing the flow into different stable fixed points as the temperature is lowered, for different host density of states profiles.

the bare coupling  $J_0$ . The LM fixed point is stable and the impurity local moment remains unscreened.

For large bare  $J_0$  the system starts off close to the particle-hole symmetric strong coupling fixed point of the linear pseudogap Kondo model, dubbed  $SSC_{Dirac}$ . In this regime, the impurity entropy is  $S_{imp} = 2 \ln 2$ . However, this fixed point is unstable and RG flow on reducing the temperature tends towards the LM fixed point with entropy  $S_{imp} = \ln 2$ . Unlike the other cases considered, here the renormalized running coupling  $J(\Lambda)$  *decreases* on reducing temperature, so that the impurity always becomes asymptotically free as  $T \rightarrow 0$ . This is illustrated in the lower panel of Fig. A.3. The Kondo effect can only be revived by doping so that the Dirac point is not longer at the fermi energy (in which case the low-energy DoS is finite and we recover the metallic scenario); or if very strong potential scattering is introduced. For the linear pseudogap case  $\rho(\omega) \sim |\omega|$  the impurity spectral function also goes as  $A(\omega) \sim |\omega|$ . Note that in this case  $\rho(\omega) \times A(\omega) \rightarrow 0$  as  $|\omega| \rightarrow 0$ , indicating a free impurity at low energies.



## A.4. Results and discussion

We now turn to our full NRG results for a magnetic impurity embedded in the TBG host. The impurity is taken to be of Anderson type (Eq. A.13), and the BM model is used for the host (Eq. A.6). The observables of primary interest are the temperature-dependence of the entropy  $S_{\text{imp}}(T)$ , and the energy-resolved impurity spectral function  $A(\omega)$  at  $T = 0$ , for TBG systems with different twist angles – see Fig. A.4. The most dramatic changes are observed in the vicinity of the magic angle at  $\theta = 1.05^\circ$ , and this is where we focus our discussion. The physical quantities we calculate reveal a complex RG flow in the system, illustrated in Fig. A.5. The physics precisely at the magic angle is also investigated in detail, and the dependence of the Kondo temperature on microscopic parameters is extracted – see Fig. A.6.

Consider first the entropy flows presented in Fig. A.4(a). At the highest temperatures  $T \sim D$ , the impurity has four thermally populated configurations (empty, doubly-occupied, and up/down spin states) and the entropy for all systems is therefore  $\ln(4)$  in this limit. On the scale  $T \sim U$  the empty and doubly-occupied impurity configurations become thermally inaccessible and only the local moment states of the impurity survive. Note that this high- $T$  charge-freezing crossover is absent in the Kondo model, which features only the two impurity spin states from the outset. Far away from the magic angle, where the low-energy TBG DoS is dominated by the linear pseudogap of the Dirac cone, the Kondo effect is inoperative and the impurity spin degrees of freedom remain unscreened down to  $T = 0$ . The impurity entropy therefore saturates at the LM value of  $\ln(2)$ . This is the basic picture for the blue line in Fig. A.4(a) obtained for twist angle  $\theta = 2^\circ$ . In the opposite limit, when the system is tuned to the magic angle  $\theta = 1.05^\circ$  the impurity physics is dominated by the power-law divergence in the low-energy DoS of TBG. The physics in this case is effectively that of the power-law Kondo model discussed in the previous section. Since  $\rho(\omega) \sim |\omega|^{-1/4}$ , the entropy saturates to  $-\frac{1}{2}\ln(2)$  for  $T \ll T_K$ , where the Kondo scale  $T_K$  itself is strongly enhanced. This is precisely what we observe for the red line in Fig. A.4(a).

However, the situation is much more complex for twist angles close to (but not at) the magic angle. To understand the full RG flow in this intermediate regime, consider Fig. A.5, together with the fixed point discussion in Sec. A.3.4 and the RG flow diagrams in Fig. A.3. Note that the same color-coding is used in Figs. A.3 and A.5.

Near the magic angle, the TBG host DoS has a compound structure featuring multiple elements, each of which corresponding to a different limiting Kondo problem. At high energies, the system shows behavior that is characteristic of the HO-vHs, denoted in blue in Fig. A.5. This behavior crosses over to that of a standard logarithmic vHs on the scale of  $E_\nu$ , denoted in green. Far below this scale, the linear vanishing pseudogap DoS of the Dirac cone emerges, denoted in red. Depending on the energy

A

window, the RG flow will therefore be controlled by the different regimes depicted in Fig. A.3.

This RG flow is reflected in the temperature dependence of the entropy. After the charge degrees of freedom are frozen out on the high-temperature scale of  $T \sim U$  and the impurity entropy reaches  $\sim \ln(2)$  characteristic of the LM regime, the system then rapidly flows towards  $\text{SSC}_{\text{HO}}$  on further reducing the temperature. On this trajectory, the effective coupling strength  $J(\Lambda)$  grows as the energy scale  $\Lambda$  decreases, and the entropy approaches  $S_{\text{imp}} = -\frac{1}{2} \ln 2$ . However, at the scale  $E_\nu$  the physics of the logarithmic vHs takes over and the system starts to flow towards the regular SC fixed point with  $S_{\text{imp}} = 0$ . The running coupling  $J(\Lambda)$  continues to increase. But on the ‘other side’ of the vHs in energy space, as the temperature is further decreased, the effect of the low-energy pseudogap DoS begins to dominate. Interestingly though, at this point in the RG flow the system already has a very strong coupling strength  $J(\Lambda)$ , which puts the system close to the unstable  $\text{SSC}_{\text{Dirac}}$  fixed point. The entropy therefore ‘overshoots’ up to  $\ln(4)$  characteristic of this fixed point. The ultimate RG flow on the lowest energy scales is therefore between  $\text{SSC}_{\text{Dirac}}$  and the stable LM fixed point of the pseudogap Kondo problem, with a residual  $T = 0$  entropy of  $\ln(2)$ . The ground state is an unscreened local moment with  $\ln(2)$  entropy in all cases except when precisely at the magic angle (where  $E_\nu = 0$  such that this final part of the flow towards LM is omitted). Our NRG results for the entropy show that the final low-temperature flow between  $\text{SSC}_{\text{Dirac}}$  and LM is controlled by an emergent energy scale  $E^* \sim |E_\nu|^3$ . As we get closer to the magic angle, the  $E_\nu$  scale reduces and the lines fold progressively onto that of the red line for the magic angle itself. The  $E^*$  scale rapidly becomes very small. This gives a finite window in twist angle over which magic angle physics can be observed at intermediate temperatures.

The same RG flow is demonstrated by the  $T = 0$  spectral function for the impurity  $A(\omega)$ , which we plot in Fig. A.4(b) for the same systems. On the lowest energy scales  $|\omega| \ll E^*$ , we find  $A(\omega) \sim |\omega|$  characteristic of the linear pseudogap Kondo model, for all cases except when precisely at the magic angle. This is because the physics here is controlled by the Dirac cone and the resulting RG flow toward the LM fixed point. By contrast, at the magic angle, the enhanced DoS leads to strong coupling physics and a flow towards the  $\text{SSC}_{\text{HO}}$  fixed point for all  $|\omega| \ll T_K$ , yielding  $A(\omega) \sim |\omega|^{1/4}$  (red line). As the magic angle is approached, the  $E_\nu$  scale diminishes and so the spectrum progressively folds onto the magic angle result, see e.g. black line for  $\theta = 1.1^\circ$  in Fig. A.4(b). The most prominent feature of the impurity spectral function is however the dramatic peak on the scale of  $E^*$  (note the log scale), which characterizes the flow between  $\text{SSC}_{\text{Dirac}}$  and LM fixed points. This is highlighted in the inset to Fig. A.4(b) which compares on a linear scale the magic angle result (red line) to systems at  $\theta = 1.6^\circ$  (orange) and  $2^\circ$  (blue). The rapid change in position and intensity of this spectral peak on nearing the magic angle demonstrates that quantum impurities

are highly sensitive probes of magic angle physics in TBG systems.

In Fig. A.6 we turn to an analysis of NRG results for systems at the magic angle itself. In the main panel (top) we plot the impurity entropy  $S_{\text{imp}}(T)$  for impurities of either Anderson type (Eq. A.13, points) or Kondo type (Eq. A.14, lines), for different impurity-host couplings.

At the highest temperatures  $T \sim D$ , the Anderson impurity again shows  $\ln(4)$  entropy for the four quasi-degenerate impurity states. At lower temperatures  $T \sim U$ , the charge configurations on the impurity in the Anderson model are frozen out and only the local moment spin states survive, giving  $\ln(2)$  entropy. In this regime the system is close to the LM fixed point. RG flow towards the  $\text{SSC}_{\text{HO}}$  strong coupling fixed point results in a crossover in the entropy on the scale of the Kondo temperature  $T \sim T_K$  to  $S_{\text{imp}} = -\frac{1}{2} \ln(2)$ . This remains the  $T = 0$  residual impurity entropy for TBG systems at the magic angle. However, the Kondo scale itself varies with the impurity-host coupling, as seen in the main panel of Fig. A.6 by the evolution of the different lines. For good scale separation  $T_K \ll U$ , we see clear two-stage behavior, with distinct crossovers to and from the LM fixed point in the Anderson model. However, given the strongly enhanced  $T_K$  at the magic angle, such a scale separation may not be in evidence in practice (see e.g. pink and orange lines in Fig. A.6 which show a more or less direct crossover in the entropy from  $\ln(4)$  to  $-\frac{1}{2} \ln(2)$ ; or indeed the cases close to the magic angle in Fig. A.4).

By contrast, the Kondo impurity features only the local moment spin configurations and hence has a  $\ln(2)$  entropy at high temperatures  $T \sim D$ . The Kondo scale generated by finite antiferromagnetic exchange coupling  $J$  results in the same crossover to the  $\text{SSC}_{\text{HO}}$  fixed point, with the same  $T = 0$  residual entropy of  $-\frac{1}{2} \ln(2)$ . Indeed, RG arguments imply [73] that the physics of the Anderson and Kondo models for  $T \ll U$  should be identical, providing the effective Kondo coupling  $J$  is chosen appropriately for a given  $U$  and  $g$  of the Anderson model. To verify this Anderson-Kondo mapping in the magic-angle TBG setting, in Fig. A.6 we considered Kondo models with different  $J$  and then fit Anderson models to match the low-temperature physics by tuning  $g$  at fixed  $U$ . In such a way, the Kondo and Anderson models have the same Kondo temperature  $T_K$ . The precise agreement in the universal regime confirms that at particle-hole symmetry the effective Kondo model is a faithful description of the more microscopic Anderson model.

The Anderson-Kondo mapping can be performed perturbatively via the approximate SW transformation [73, 101] as described in Sec. A.3. The exact relationship between  $J$  and  $g$  as extracted from our NRG results is shown in the lower left panel of Fig. A.6 as the circle points. The SW result (red dashed line) is seen to work well when the bare coupling of the underlying Anderson model is small,  $g \ll U$  (small  $T_K$  regime). Away from this limit, NRG results show that the Kondo model is still the correct low-energy

A

effective model, but that non-perturbative techniques must be used to obtain the correct effective model parameters [102]. The evolution of the numerically-extracted Kondo temperature as a function of the effective  $J$  is shown in the lower right panel of Fig. A.6 (points), and is compared with the analytic result for the Kondo model Eq. A.25 (red dashed line). The blue dotted line is the asymptotic small- $J$  limit of this expression,  $T_K \sim (4\rho_0 J)^{1/\alpha}$ .

Our full NRG results for an impurity in magic angle TBG therefore confirm the analytic predictions of the previous sections. For a comparison with results for an impurity coupled to a standard logarithmic vHs, see Appendix C.

Finally, we comment on the role of potential scattering and particle-hole symmetry breaking. In the above analysis we have for simplicity neglected particle-hole asymmetry in the TBG host DoS by employing the symmetric BM model. However, we believe this approximation is well-justified and does not affect the presented results. Although in principle particle-hole asymmetry can lead to Kondo screening in the linear pseudogap case [78] relevant to the low-energy Dirac cone in TBG away from the magic angle, the singlet-doublet quantum phase transition arises only at very strong asymmetry. In practice, the relatively small particle-hole symmetry breaking in TBG means that the impurity problem is far away from the asymmetric strong coupling Kondo phase. Within the doublet local moment phase, particle-hole asymmetry is RG irrelevant and can be safely ignored. We have also assumed that the impurity itself is particle-hole symmetric ( $\epsilon_d = -U_d/2$  in the Anderson model, or  $V = 0$  in the Kondo model). Relaxing this condition induces potential scattering in the TBG host. Very strong deviations away from the half-filled Anderson impurity are required to destroy the local moment ground state (the resulting asymmetric Kondo strong coupling state is continuously connected to the trivial empty orbital state of the impurity). In this regime, the mapping to the Kondo model breaks down (the large value of  $V$  in the Kondo model required for Kondo screening is unphysical). Therefore, we argue that the results presented above are generic for a local moment impurity embedded in a TBG host material.

## A.5. Conclusions

In this paper, we have studied the physics of a single magnetic impurity in TBG at, and close to, the magic angle. We find a surprisingly rich range of behavior, rooted in the unique evolution of the TBG density of states. It is interesting to note that there is no Kondo screened ground state in general, only at the magic angle. However, the signatures at finite temperature relevant to experiment show highly non-trivial structure due to the interplay between van Hove and Dirac physics on the level of a strongly correlated quantum impurity problem. Close to the magic angle, the TBG host density of states at different energy scales yields different limits of

paradigmatic Kondo models – from logarithmic and power-law diverging Kondo to pseudogap vanishing Kondo. The subtle renormalization group flow between these limits shows up in the temperature and energy dependence of physical observables.

The behavior we uncover should be detectable in STM experiments. Indeed we argue that the impurity response in TBG gives a very clear signature of magic angle physics. Magnetic impurities may therefore prove useful as highly sensitive *in-situ* probes for moiré materials.

An interesting direction of future research is the role of the RKKY interaction between multiple magnetic impurities in TBG, and how it competes with the Kondo effect of individual impurities near the magic angle.

Although van Hove-boostered Kondo physics may be observable in other systems (including 3d bulk metals [126, 127] with magnetic impurities), we note that TBG stands out as a uniquely tunable platform. Furthermore, TBG also allows one to study the complex interplay of these effects with Dirac physics.

## acknowledgments

We thank S. Polla, V. Cheianov, L. Classen, A. Chubukov, and L. Fu for helpful discussions. this work is part of the D-ITP consortium, a program of the Netherlands Organisation for Scientific Research (NWO) that is funded by the Dutch Ministry of Education, Culture and Science (OCW). DOO acknowledges the support from the Netherlands Organization for Scientific Research (NWO/OCW) and from the European Research Council (ERC) under the European Union's Horizon 2020 research and innovation programme. AKM acknowledges funding from the Irish Research Council through the Laureate Award 2017/2018 grant IRCLA/2017/169.

## .1. Locating saddle point positions in the particle-hole symmetric BM model

To locate the saddle points in the Brillouin zone, we require gradients of the energy. The flat bands make it imperative that the first derivative is computed very accurately, and this means that we must avoid crude finite difference methods for numerical derivatives of the energy. This problem can be addressed by utilizing our analytical access to the Hamiltonian itself, and implementing the Hellman-Feynman theorem,

$$\frac{\partial E}{\partial k^i} = \langle \psi_k | \frac{\partial H}{\partial k^i} | \psi_k \rangle, \quad (26)$$

where  $\psi_{\mathbf{k}}$  is the wavefunction of the lowest positive energy band at momentum  $\mathbf{k}$ . A more extended analysis of this method has been introduced recently in [128].

The saddle point is found by minimizing the value of  $(\partial_{k_x}\epsilon_{\mathbf{k}})^2 + (\partial_{k_y}\epsilon_{\mathbf{k}})^2$  over the Brillouin zone vectors, by using the conjugate gradient method. The coefficients for the local energy dispersion are then calculated along the principal directions of the saddle point. These directions are given by the eigenvectors of the Hessian matrix, and are in general different from the  $k_x$  and  $k_y$  of the Brillouin zone. Derivatives are convenient to compute along the natural Brillouin zone directions, however. The trick to overcome this is to note that a matrix formed from  $n$  derivatives of a scalar transforms like a rank- $n$  tensor. Then the tensor transformation rule can be used with a covariant Jacobian to obtain the coefficients along the rotated axes.

One subtlety is that for angles very close to the magic angle, there are secondary vHs points at other locations in the Brillouin zone than those indicated in Fig. A.2a. For the purposes of the Kondo effect, we have only considered the one with the largest spectral weight, since this is found to dominate the results of our NRG calculations. This is done by computing the local dispersion coefficients  $\alpha$  and  $\beta$  at each of the saddle points, and picking the one with the largest value of  $\frac{1}{\sqrt{\alpha\beta}}$ .

## .2. Mapping from TBG density of states to the NRG Wilson chain

The TBG DoS away from the magic angle has two qualitative features: the linear-pseudogap Dirac cone at low energies and the divergence due to the vHs on the scale of  $E_V$ . We extract an effective model DoS from analysis of the BM model for different twist angles – see left panels of Fig. 7 for the cases explicitly considered in the main text (we have rescaled the energy range in terms of the bandwidth cutoff and normalized the spectrum to unity). This DoS is then discretized logarithmically and mapped to a Wilson chain [105] as described in Sec. A.3.2. The corresponding Wilson chain hopping parameters are plotted in the right panels of Fig. 7. The results show that the different DoS elements can be captured in NRG through the crossover behavior in the functional form of the Wilson chain.

## .3. NRG calculations for an impurity coupled to a conventional log-vHs host

In Fig. 8 we provide reference NRG calculations for a Kondo impurity coupled to a pure log-diverging DoS. This gives a useful comparison to our result for an impurity

embedded in the magic-angle TBG system, which has a HO-vHs point and hence a stronger power-law diverging DoS. As predicted from our perturbative scaling (poor man's scaling) results, the system flows towards strong coupling in all cases, in which the impurity is Kondo-screened. The residual entropy at  $T = 0$  is seen to be  $S_{\text{imp}} = 0$ , although this limit is approached logarithmically slowly from below. This is characteristic of the logarithmic DoS. From the scaling with bare coupling strength  $J$  in the left panel, the Kondo temperature  $T_K$  is seen to be enhanced relative to the metallic case, but substantially suppressed relative to the power-law diverging DoS case. In the right panel, we analyze the behavior of  $T_K$  in more detail, comparing NRG results at different  $J$  (circle points) with our analytic formula Eq. A.24 (black line). The results agree almost perfectly. The red dashed line is the asymptotic result at small  $J$ , which also does remarkably well compared with exact NRG results.

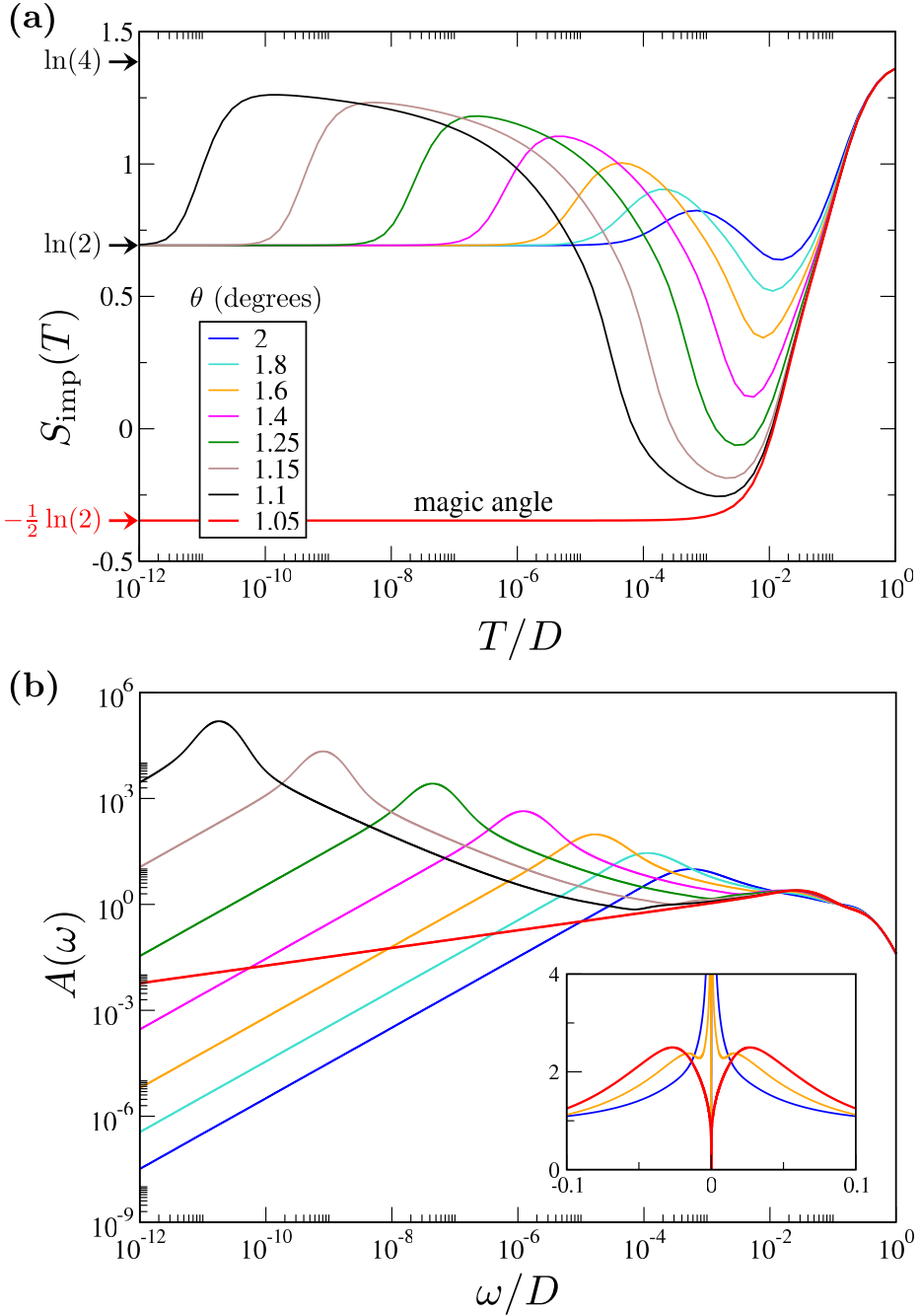


Figure A.4: NRG results for an Anderson impurity in the TBG host material described by the BM model, at various twist angles  $\theta$  approaching the magic angle at  $\theta = 1.05^\circ$ . (a) Impurity entropy  $S_{\text{imp}}(T)$  vs temperature  $T$ ; and (b) Impurity spectral function  $A(\omega)$  vs energy  $\omega$  at  $T = 0$ . Inset shows low-energy spectral details on a linear scale for representative cases approaching the magic angle. All plots shown for  $U_d = 0.4D$ ,  $\epsilon_d = -U_d/2$  and  $g = 0.2D$ , with  $D$  the TBG bandwidth.



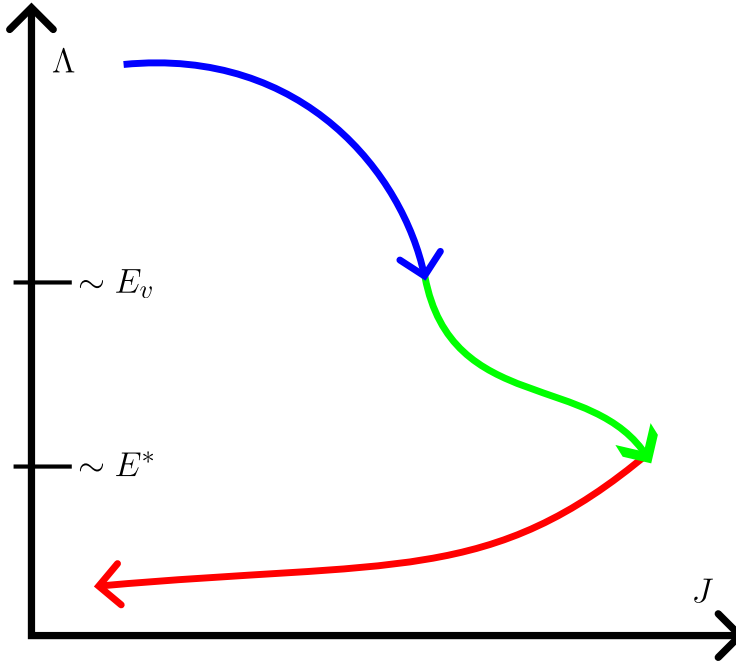


Figure A.5: Near the magic angle, the TBG host DoS has a compound structure. At high energies  $\Lambda$ , the power-law diverging DoS associated with the HO-vHs generates a rapid RG flow towards strong coupling – blue arrow. On the scale of  $E_v$  the DoS crosses over to logarithmic vHs – green arrow. Below  $E_v$  the Dirac cone pseudogap dominates the DoS and  $J(\Lambda)$  begins to decrease again as the system flows back towards the free local moment regime on an emergent scale  $E^*$ . The color-coding is the same as that in Fig. A.3.

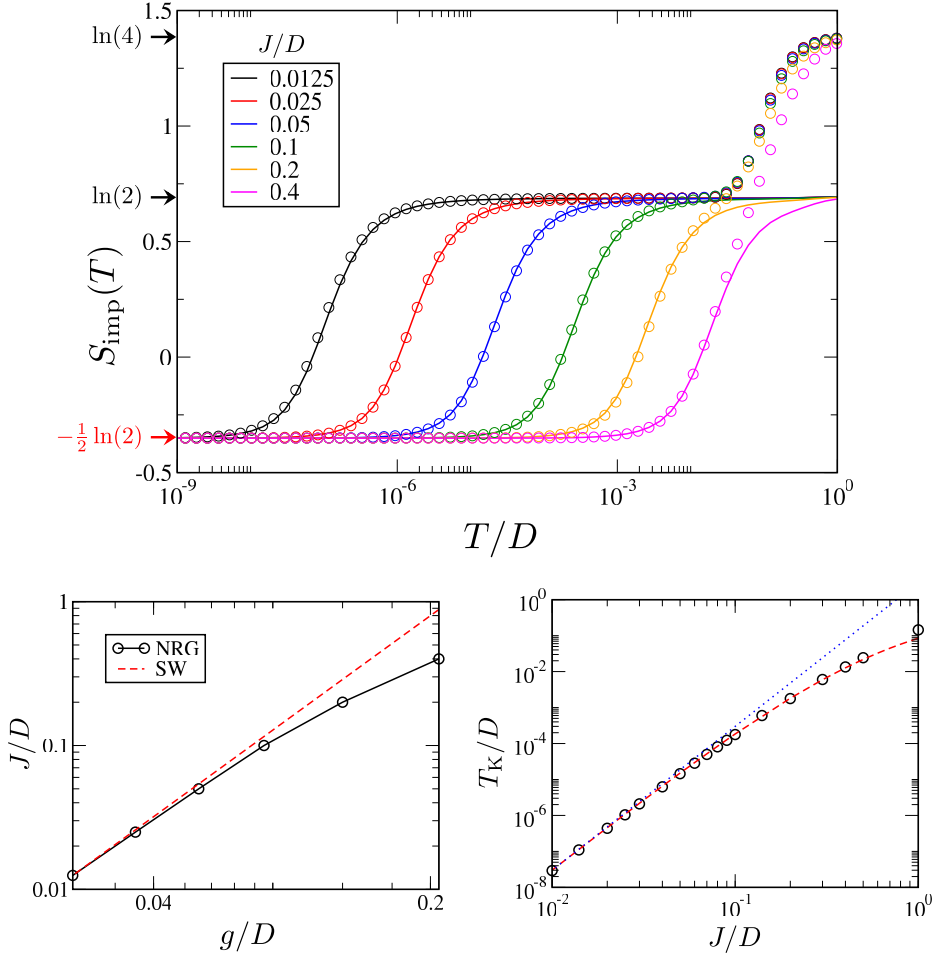


Figure A.6: NRG results for an impurity embedded in magic angle TBG. Main panel: Entropy  $S_{\text{imp}}$  vs  $T$  for Anderson and Kondo impurities (points and lines respectively) for different impurity-host couplings. For a given Kondo  $J$ , the low temperature physics of an Anderson model with fixed  $U = 0.4D$  is fit by tuning  $g$ . The relationship between  $J$  and  $g$  is shown in the lower-left inset (points), comparing with the SW result (red dashed line). The evolution of  $T_K$  with  $J$  is shown in the lower-right inset (points), comparing with Eq. A.25 (red dashed line) and its small- $J$  asymptote (blue dotted line).  $T_K$  is extracted numerically from NRG results for the entropy, defined in practice via  $S_{\text{imp}}(T = T_K) = 0$ .

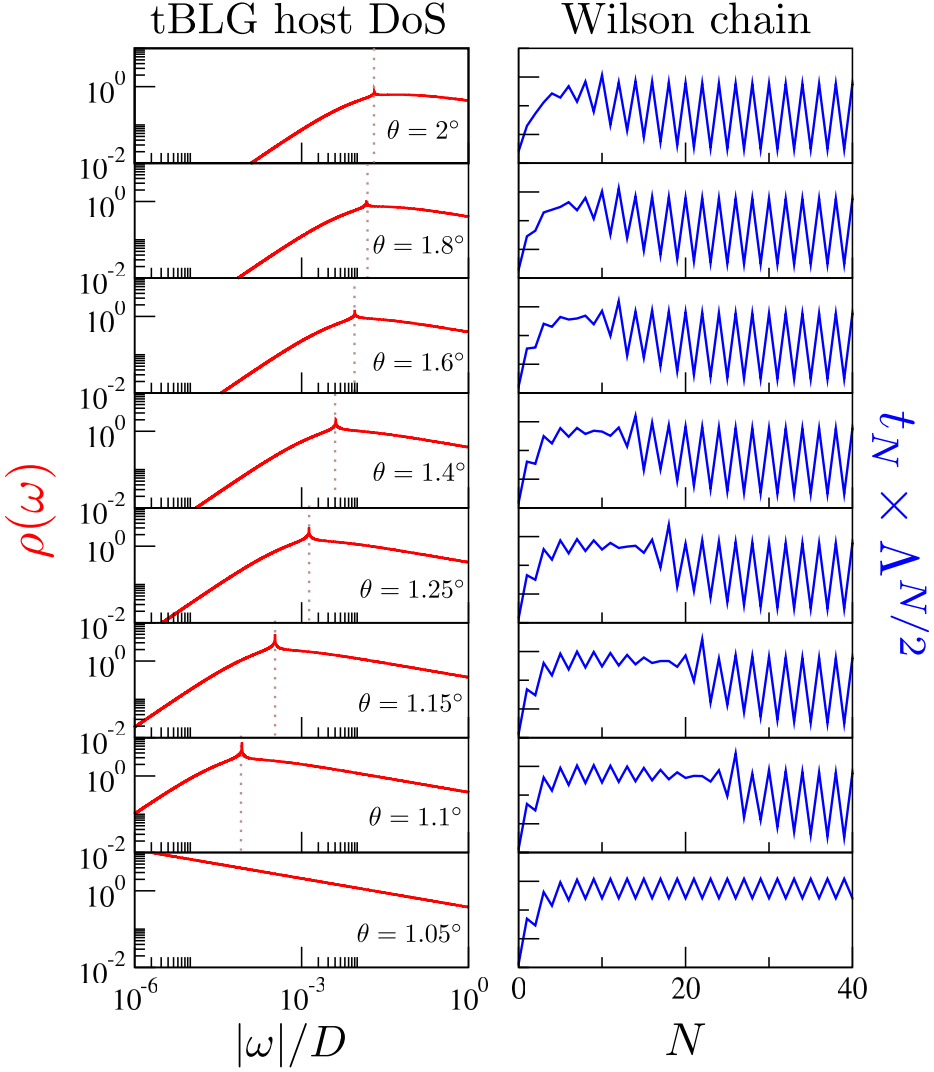


Figure 7: Left panels: DoS used in our NRG calculations, obtained from analysis of the effective BM model, for different twist angles  $\theta$  as used in the main text. Vertical dotted lines show the  $E_v$  scale at which the vHs divergence occurs. This scale moves to lower energies as the magic angle is approached. Right panels: corresponding Wilson chain coefficients.

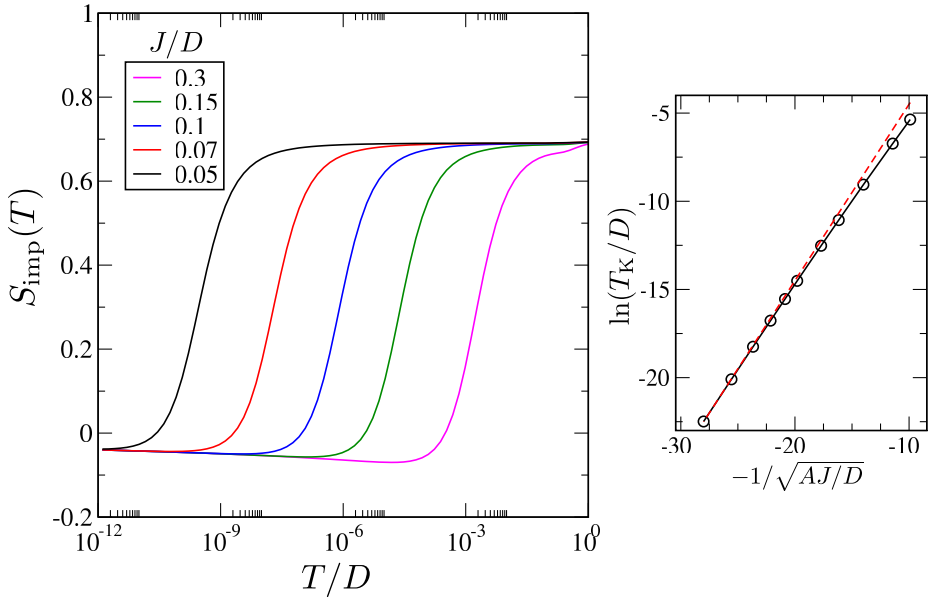


Figure 8: Main panel: NRG results for the impurity entropy  $S_{\text{imp}}$  vs temperature  $T$  for different bare coupling strengths  $J$ , in a system with a pure log-diverging DoS (standard vHs). Right inset shows the extracted  $T_K$  scale (points), compared with Eq. A.24 (black line) and the asymptotic result  $T_K \sim D e^{-1/\sqrt{AJ/D}}$  (red dashed line), with  $A = a\rho_0 D/2$ .

## Bibliography

- [1] D. Chowdhury, A. Georges, O. Parcollet, and S. Sachdev, *Sachdev-ye-kitaev models and beyond: Window into non-fermi liquids*, *Rev. Mod. Phys.* **94** (Sep, 2022) 035004.
- [2] V. Rosenhaus, *An introduction to the syk model*, *Journal of Physics A: Mathematical and Theoretical* **52** (2019), no. 32 323001.
- [3] M. Franz and M. Rozali, *Mimicking black hole event horizons in atomic and solid-state systems*, *Nature Reviews Materials* **3** (2018), no. 12 491–501.
- [4] A. A. Patel and S. Sachdev, *Quantum chaos on a critical Fermi surface*, *Proceedings of the National Academy of Sciences* **114** (Feb., 2017) 1844–1849. arXiv: 1611.00003.
- [5] M. Tikhanovskaya, S. Sachdev, and A. A. Patel, *Maximal quantum chaos of the critical fermi surface*, *arXiv preprint arXiv:2202.01845* (2022).
- [6] J. Maldacena and D. Stanford, *Comments on the Sachdev-Ye-Kitaev model*, *Physical Review D* **94** (Nov., 2016) 106002. arXiv: 1604.07818.
- [7] J. Polchinski and V. Rosenhaus, *The Spectrum in the Sachdev-Ye-Kitaev Model*, *Journal of High Energy Physics* **2016** (Apr., 2016) 1–25. arXiv: 1601.06768.
- [8] D. I. Pikulin and M. Franz, *Black hole on a chip: Proposal for a physical realization of the sachdev-ye-kitaev model in a solid-state system*, *Phys. Rev. X* **7** (Jul, 2017) 031006.
- [9] A. Chew, A. Essin, and J. Alicea, *Approximating the sachdev-ye-kitaev model with majorana wires*, *Phys. Rev. B* **96** (Sep, 2017) 121119.
- [10] A. Chen, R. Ilan, F. de Juan, D. I. Pikulin, and M. Franz, *Quantum holography in a graphene flake with an irregular boundary*, *Phys. Rev. Lett.* **121** (Jul, 2018) 036403.
- [11] O. Can, E. M. Nica, and M. Franz, *Charge transport in graphene-based mesoscopic realizations of Sachdev-Ye-Kitaev models*, *Physical Review B* **99** (Jan., 2019) 045419. arXiv: 1808.06584.
- [12] I. Danshita, M. Hanada, and M. Tezuka, *Creating and probing the sachdev-ye-kitaev model with ultracold gases: Towards experimental studies of quantum gravity*, *Progress of Theoretical and Experimental Physics* **2017** (2017), no. 8.
- [13] C. Wei and T. A. Sedrakyan, *Optical lattice platform for the sachdev-ye-kitaev model*, *Physical Review A* **103** (2021), no. 1 013323.

- [14] J. Zaanen, *Planckian dissipation, minimal viscosity and the transport in cuprate strange metals*, *SciPost Physics* **6** (May, 2019) 061.
- [15] S. A. Hartnoll and A. P. Mackenzie, *Planckian dissipation in metals*, 2021.
- [16] A. A. Patel, J. McGreevy, D. P. Arovas, and S. Sachdev, *Magnetotransport in a Model of a Disordered Strange Metal*, *Physical Review X* **8** (May, 2018) 021049.
- [17] S. A. Hartnoll and A. P. Mackenzie, *Colloquium: Planckian dissipation in metals*, *Reviews of Modern Physics* **94** (2022), no. 4 041002.
- [18] Y. Gu and A. Kitaev, *On the relation between the magnitude and exponent of otocs*, *Journal of High Energy Physics* **2019** (2019), no. 2 1–21.
- [19] A. I. Larkin and Y. N. Ovchinnikov, *Quasiclassical method in the theory of superconductivity*, *Sov Phys JETP* **28** (1969), no. 6 1200–1205.
- [20] K. Hashimoto, K. Murata, and R. Yoshii, *Out-of-time-order correlators in quantum mechanics*, *Journal of High Energy Physics* **2017** (Oct., 2017) 138. arXiv: 1703.09435.
- [21] B. Kobrin, Z. Yang, G. D. Kahanamoku-Meyer, C. T. Olund, J. E. Moore, D. Stanford, and N. Y. Yao, *Many-Body Chaos in the Sachdev-Ye-Kitaev Model*, *Physical Review Letters* **126** (Jan., 2021) 030602. arXiv: 2002.05725.
- [22] B. Craps, M. De Clerck, D. Janssens, V. Luyten, and C. Rabideau, *Lyapunov growth in quantum spin chains*, *Physical Review B* **101** (May, 2020) 174313. arXiv: 1908.08059.
- [23] D. Stanford, *Many-body chaos at weak coupling*, *Journal of High Energy Physics* **2016** (Oct., 2016) 9. arXiv: 1512.07687.
- [24] J. Maldacena, S. H. Shenker, and D. Stanford, *A bound on chaos*, *Journal of High Energy Physics* **2016** (Aug., 2016) 106. arXiv: 1503.01409.
- [25] M. Fremling, M. Haque, and L. Fritz, *Bipartite sachdev-ye-kitaev model: Conformal limit and level statistics*, *Physical Review D* **105** (mar, 2022).
- [26] M. Fremling and L. Fritz, *A bipartite variant of the Sachdev-Ye-Kitaev model from a strained Kitaev honeycomb model*, *arXiv:2105.06119 [cond-mat]* (May, 2021). arXiv: 2105.06119.
- [27] É. Lantagne-Hurtubise, S. Plugge, O. Can, and M. Franz, *Diagnosing quantum chaos in many-body systems using entanglement as a resource*, *Physical Review Research* **2** (2020), no. 1 013254.
- [28] J. Kim, I. R. Klebanov, G. Tarnopolsky, and W. Zhao, *Symmetry breaking in coupled SYK or tensor models*, *Phys. Rev. X* **9** (May, 2019) 021043.

- [29] S. Sahoo, E. Lantagne-Hurtubise, S. Plugge, and M. Franz, *Traversable wormhole and Hawking-Page transition in coupled complex SYK models*, *Physical Review Research* **2** (Oct., 2020) 043049.
- [30] D. Chowdhury, Y. Werman, E. Berg, and T. Senthil, *Translationally Invariant Non-Fermi-Liquid Metals with Critical Fermi Surfaces: Solvable Models*, *Physical Review X* **8** (July, 2018) 031024.
- [31] D. J. Gross and V. Rosenhaus, *A Generalization of Sachdev-Ye-Kitaev*, *Journal of High Energy Physics* **2017** (Feb., 2017) 93. arXiv: 1610.01569.
- [32] E. Marcus and S. Vandoren, *A new class of SYK-like models with maximal chaos*, *Journal of High Energy Physics* **2019** (2019), no. 1 166.
- [33] A. M. Garcia-Garcia, Y. Jia, D. Rosa, and J. J. Verbaarschot, *Sparse Sachdev-Ye-Kitaev model, quantum chaos, and gravity duals*, *Physical Review D* **103** (May, 2021) 106002.
- [34] S. Xu, L. Susskind, Y. Su, and B. Swingle, *A Sparse Model of Quantum Holography*, Aug., 2020. Number: arXiv:2008.02303 arXiv:2008.02303 [cond-mat, physics:hep-th, physics:quant-ph].
- [35] O. Parcollet and A. Georges, *Non-Fermi-liquid regime of a doped Mott insulator*, *Physical Review B* **59** (Feb., 1999) 5341–5360.
- [36] Y. Gu, A. Kitaev, S. Sachdev, and G. Tarnopolsky, *Notes on the complex Sachdev-Ye-Kitaev model*, *Journal of High Energy Physics* **2020** (Feb., 2020) 157.
- [37] S. Plugge, E. Lantagne-Hurtubise, and M. Franz, *Revival dynamics in a traversable wormhole*, *Phys. Rev. Lett.* **124** (Jun, 2020) 221601.
- [38] A. Romero-Bermúdez, K. Schalm, and V. Scopelliti, *Regularization dependence of the otoc. which lyapunov spectrum is the physical one?*, *Journal of High Energy Physics* **2019** (2019), no. 7 1–32.
- [39] Y. Chen, H. Zhai, and P. Zhang, *Tunable quantum chaos in the sachdev-ye-kitaev model coupled to a thermal bath*, *Journal of High Energy Physics* **2017** (2017), no. 7 1–28.
- [40] J. M. B. Lopes dos Santos, N. M. R. Peres, and A. H. Castro Neto, *Graphene bilayer with a twist: Electronic structure*, *Phys. Rev. Lett.* **99** (Dec, 2007) 256802.
- [41] E. Suárez Morell, J. D. Correa, P. Vargas, M. Pacheco, and Z. Barticevic, *Flat bands in slightly twisted bilayer graphene: Tight-binding calculations*, *Phys. Rev. B* **82** (Sep, 2010) 121407.

- [42] R. Bistritzer and A. H. MacDonald, *Moiré bands in twisted double-layer graphene*, *Proceedings of the National Academy of Sciences* **108** (2011), no. 30 12233–12237.
- [43] K. Kim, A. DaSilva, S. Huang, B. Fallahazad, S. Larentis, T. Taniguchi, K. Watanabe, B. J. LeRoy, A. H. MacDonald, and E. Tutuc, *Tunable moiré bands and strong correlations in small-twist-angle bilayer graphene*, *Proceedings of the National Academy of Sciences* **114** (2017), no. 13 3364–3369.
- [44] J. Liu, J. Liu, and X. Dai, *Pseudo landau level representation of twisted bilayer graphene: Band topology and implications on the correlated insulating phase*, *Phys. Rev. B* **99** (Apr, 2019) 155415.
- [45] N. F. Q. Yuan, H. Isobe, and L. Fu, *Magic of high-order van Hove singularity*, *Nature Communications* **10** (Dec., 2019) 5769.
- [46] Z. Song, Z. Wang, W. Shi, G. Li, C. Fang, and B. A. Bernevig, *All magic angles in twisted bilayer graphene are topological*, *Phys. Rev. Lett.* **123** (Jul, 2019) 036401.
- [47] G. Tarnopolsky, A. J. Kruchkov, and A. Vishwanath, *Origin of magic angles in twisted bilayer graphene*, *Phys. Rev. Lett.* **122** (Mar, 2019) 106405.
- [48] Y. Cao, V. Fatemi, S. Fang, K. Watanabe, T. Taniguchi, E. Kaxiras, and P. Jarillo-Herrero, *Unconventional superconductivity in magic-angle graphene superlattices*, *Nature* **556** (Apr., 2018) 43–50.
- [49] Y. Cao, V. Fatemi, A. Demir, S. Fang, S. L. Tomarken, J. Y. Luo, J. D. Sanchez-Yamagishi, K. Watanabe, T. Taniguchi, E. Kaxiras, R. C. Ashoori, and P. Jarillo-Herrero, *Correlated insulator behaviour at half-filling in magic-angle graphene superlattices*, *Nature* **556** (Apr., 2018) 80–84.
- [50] X. Lu, P. Stepanov, W. Yang, M. Xie, M. A. Aamir, I. Das, C. Urgell, K. Watanabe, T. Taniguchi, G. Zhang, A. Bachtold, A. H. MacDonald, and D. K. Efetov, *Superconductors, orbital magnets and correlated states in magic-angle bilayer graphene*, *Nature* **574** (Oct., 2019) 653–657.
- [51] R. Ojajärvi, T. Hyart, M. A. Silaev, and T. T. Heikkilä, *Competition of electron-phonon mediated superconductivity and stoner magnetism on a flat band*, *Phys. Rev. B* **98** (Aug, 2018) 054515.
- [52] H. Isobe, N. F. Q. Yuan, and L. Fu, *Unconventional superconductivity and density waves in twisted bilayer graphene*, *Phys. Rev. X* **8** (Dec, 2018) 041041.
- [53] F. Wu, A. H. MacDonald, and I. Martin, *Theory of phonon-mediated superconductivity in twisted bilayer graphene*, *Phys. Rev. Lett.* **121** (Dec, 2018) 257001.



- [54] T. J. Peltonen, R. Ojajärvi, and T. T. Heikkilä, *Mean-field theory for superconductivity in twisted bilayer graphene*, *Phys. Rev. B* **98** (Dec, 2018) 220504.
- [55] V. Kozii, H. Isobe, J. W. F. Venderbos, and L. Fu, *Nematic superconductivity stabilized by density wave fluctuations: Possible application to twisted bilayer graphene*, *Phys. Rev. B* **99** (Apr, 2019) 144507.
- [56] M. Yankowitz, S. Chen, H. Polshyn, Y. Zhang, K. Watanabe, T. Taniguchi, D. Graf, A. F. Young, and C. R. Dean, *Tuning superconductivity in twisted bilayer graphene*, *Science* **363** (2019), no. 6431 1059–1064.
- [57] T. Hazra, N. Verma, and M. Randeria, *Bounds on the superconducting transition temperature: Applications to twisted bilayer graphene and cold atoms*, *Phys. Rev. X* **9** (Sep, 2019) 031049.
- [58] X. Hu, T. Hyart, D. I. Pikulin, and E. Rossi, *Geometric and conventional contribution to the superfluid weight in twisted bilayer graphene*, *Phys. Rev. Lett.* **123** (Dec, 2019) 237002.
- [59] F. Xie, Z. Song, B. Lian, and B. A. Bernevig, *Topology-bounded superfluid weight in twisted bilayer graphene*, *Phys. Rev. Lett.* **124** (Apr, 2020) 167002.
- [60] A. Julku, T. J. Peltonen, L. Liang, T. T. Heikkilä, and P. Törmä, *Superfluid weight and berezinskii-kosterlitz-thouless transition temperature of twisted bilayer graphene*, *Phys. Rev. B* **101** (Feb, 2020) 060505.
- [61] L. Van Hove, *The occurrence of singularities in the elastic frequency distribution of a crystal*, *Phys. Rev.* **89** (Mar, 1953) 1189–1193.
- [62] G. Li, A. Luican, J. M. B. Lopes dos Santos, A. H. Castro Neto, A. Reina, J. Kong, and E. Y. Andrei, *Observation of van Hove singularities in twisted graphene layers*, *Nature Physics* **6** (Feb, 2010) 109–113.
- [63] L. Classen, A. V. Chubukov, C. Honerkamp, and M. M. Scherer, *Competing orders at higher-order van hove points*, *Phys. Rev. B* **102** (Sep, 2020) 125141.
- [64] A. Kerelsky, L. J. McGilly, D. M. Kennes, L. Xian, M. Yankowitz, S. Chen, K. Watanabe, T. Taniguchi, J. Hone, C. Dean, A. Rubio, and A. N. Pasupathy, *Maximized electron interactions at the magic angle in twisted bilayer graphene*, *Nature* **572** (Aug, 2019) 95–100.
- [65] Y. Choi, J. Kemmer, Y. Peng, A. Thomson, H. Arora, R. Polski, Y. Zhang, H. Ren, J. Alicea, G. Refael, F. von Oppen, K. Watanabe, T. Taniguchi, and S. Nadj-Perge, *Electronic correlations in twisted bilayer graphene near the magic angle*, *Nature Physics* **15** (Nov, 2019) 1174–1180.

- [66] M. Crommie, C. P. Lutz, and D. Eigler, *Imaging standing waves in a two-dimensional electron gas*, *Nature* **363** (1993), no. 6429 524–527.
- [67] T. Jamneala, V. Madhavan, W. Chen, and M. F. Crommie, *Scanning tunneling spectroscopy of transition-metal impurities at the surface of gold*, *Physical Review B* **61** (2000), no. 15 9990.
- [68] V. Madhavan, W. Chen, T. Jamneala, M. F. Crommie, and N. S. Wingreen, *Local spectroscopy of a kondo impurity: Co on au (111)*, *Physical Review B* **64** (2001), no. 16 165412.
- [69] J. Hoffman, K. McElroy, D.-H. Lee, K. Lang, H. Eisaki, S. Uchida, and J. Davis, *Imaging quasiparticle interference in  $\text{Bi}_2\text{Sr}_2\text{CaCu}_2\text{O}_{8+\delta}$* , *Science* **297** (2002), no. 5584 1148–1151.
- [70] T. Costi, L. Bergqvist, A. Weichselbaum, J. von Delft, T. Micklitz, A. Rosch, P. Mavropoulos, P. H. Dederichs, F. Mallet, L. Saminadayar, et al., *Kondo decoherence: finding the right spin model for iron impurities in gold and silver*, *Physical review letters* **102** (2009), no. 5 056802.
- [71] M. Ternes, A. J. Heinrich, and W.-D. Schneider, *Spectroscopic manifestations of the kondo effect on single adatoms*, *Journal of Physics: Condensed Matter* **21** (2008), no. 5 053001.
- [72] L. Bogani and W. Wernsdorfer, *Molecular spintronics using single-molecule magnets*, *Nature materials* **7** (2008), no. 3 179–186.
- [73] A. C. Hewson, *The Kondo Problem to Heavy Fermions*. Cambridge Studies in Magnetism. Cambridge University Press, 1993.
- [74] P. G. Derry, A. K. Mitchell, and D. E. Logan, *Quasiparticle interference from magnetic impurities*, *Physical Review B* **92** (2015), no. 3 035126.
- [75] G. Mihailescu, S. Campbell, and A. K. Mitchell, *Thermometry of strongly correlated fermionic quantum systems using impurity probes*, *Physical Review A* **107** (2023), no. 4 042614.
- [76] J.-H. Chen, L. Li, W. G. Cullen, E. D. Williams, and M. S. Fuhrer, *Tunable kondo effect in graphene with defects*, *Nature Physics* **7** (2011), no. 7 535–538.
- [77] M. Vojta, L. Fritz, and R. Bulla, *Gate-controlled kondo screening in graphene: Quantum criticality and electron-hole asymmetry*, *EPL (Europhysics Letters)* **90** (2010), no. 2 27006.
- [78] L. Fritz and M. Vojta, *The physics of Kondo impurities in graphene*, *Reports on Progress in Physics* **76** (feb, 2013) 032501.

- [79] A. K. Mitchell and L. Fritz, *Kondo effect with diverging hybridization: Possible realization in graphene with vacancies*, *Physical Review B* **88** (2013), no. 7 075104.
- [80] A. K. Mitchell, D. Schuricht, M. Vojta, and L. Fritz, *Kondo effect on the surface of three-dimensional topological insulators: Signatures in scanning tunneling spectroscopy*, *Physical Review B* **87** (2013), no. 7 075430.
- [81] A. K. Mitchell and L. Fritz, *Kondo effect in three-dimensional dirac and weyl systems*, *Physical Review B* **92** (2015), no. 12 121109.
- [82] J. Martinek, Y. Utsumi, H. Imamura, J. Barnaś, S. Maekawa, J. König, and G. Schön, *Kondo effect in quantum dots coupled to ferromagnetic leads*, *Physical review letters* **91** (2003), no. 12 127203.
- [83] M. R. Calvo, J. Fernandez-Rossier, J. J. Palacios, D. Jacob, D. Natelson, and C. Untiedt, *The kondo effect in ferromagnetic atomic contacts*, *Nature* **458** (2009), no. 7242 1150–1153.
- [84] E. Müller-Hartmann and J. Zittartz, *Kondo effect in superconductors*, *Physical Review Letters* **26** (1971), no. 8 428.
- [85] A. Polkovnikov, S. Sachdev, and M. Vojta, *Impurity in a d-wave superconductor: Kondo effect and stm spectra*, *Physical Review Letters* **86** (2001), no. 2 296.
- [86] A. Kolezhuk, S. Sachdev, R. R. Biswas, and P. Chen, *Theory of quantum impurities in spin liquids*, *Physical Review B* **74** (2006), no. 16 165114.
- [87] M. Vojta, A. K. Mitchell, and F. Zschöcke, *Kondo impurities in the kitaev spin liquid: Numerical renormalization group solution and gauge-flux-driven screening*, *Physical review letters* **117** (2016), no. 3 037202.
- [88] W.-Y. He and P. A. Lee, *Magnetic impurity as a local probe of the  $U(1)$  quantum spin liquid with spinon fermi surface*, *Physical Review B* **105** (2022), no. 19 195156.
- [89] D. May, P.-W. Lo, K. Deltenre, A. Henke, J. Mao, Y. Jiang, G. Li, E. Y. Andrei, G.-Y. Guo, and F. B. Anders, *Modeling of the gate-controlled kondo effect at carbon point defects in graphene*, *Phys. Rev. B* **97** (Apr, 2018) 155419.
- [90] Z.-D. Song and B. A. Bernevig, *Magic-angle twisted bilayer graphene as a topological heavy fermion problem*, *Physical review letters* **129** (2022), no. 4 047601.
- [91] H. Hu, B. A. Bernevig, and A. M. Tsvelik, *Kondo lattice model of magic-angle twisted-bilayer graphene: Hund's rule, local-moment fluctuations, and low-energy effective theory*, *arXiv preprint arXiv:2301.04669* (2023).

- [92] H. Hu, G. Rai, L. Crippa, J. Herzog-Arbeitman, D. Călugăru, T. Wehling, G. Sangiovanni, R. Valenti, A. Tsvelik, and B. Bernevig, *Symmetric kondo lattice states in doped strained twisted bilayer graphene*, *arXiv preprint arXiv:2301.04673* (2023).
- [93] G.-D. Zhou and Z.-D. Song, *Kondo resonance, pomeranchuk effect, and heavy fermi liquid in twisted bilayer graphene—a numerical renormalization group study*, *arXiv preprint arXiv:2301.04661* (2023).
- [94] B. Lian, Z. Wang, and B. A. Bernevig, *Twisted bilayer graphene: A phonon-driven superconductor*, *Phys. Rev. Lett.* **122** (Jun, 2019) 257002.
- [95] A. Chandrasekaran, A. Shtyk, J. J. Betouras, and C. Chamon, *Catastrophe theory classification of fermi surface topological transitions in two dimensions*, *Phys. Rev. Research* **2** (Mar, 2020) 013355.
- [96] N. F. Q. Yuan and L. Fu, *Classification of critical points in energy bands based on topology, scaling, and symmetry*, *Phys. Rev. B* **101** (Mar, 2020) 125120.
- [97] J. Kondo, *Theory of dilute magnetic alloys*, in *Solid State Physics*, pp. 183–281. Elsevier, 1970.
- [98] A. Bayat, P. Sodano, and S. Bose, *Negativity as the entanglement measure to probe the kondo regime in the spin-chain kondo model*, *Physical Review B* **81** (2010), no. 6 064429.
- [99] A. K. Mitchell, M. Becker, and R. Bulla, *Real-space renormalization group flow in quantum impurity systems: Local moment formation and the kondo screening cloud*, *Physical Review B* **84** (2011), no. 11 115120.
- [100] I. V Borzenets, J. Shim, J. C. Chen, A. Ludwig, A. D. Wieck, S. Tarucha, H.-S. Sim, and M. Yamamoto, *Observation of the kondo screening cloud*, *Nature* **579** (2020), no. 7798 210–213.
- [101] J. R. Schrieffer and P. A. Wolff, *Relation between the anderson and kondo hamiltonians*, *Physical Review* **149** (1966), no. 2 491.
- [102] J. B. Rigo and A. K. Mitchell, *Machine learning effective models for quantum systems*, *Physical Review B* **101** (2020), no. 24 241105.
- [103] P. Anderson, *A poor man's derivation of scaling laws for the kondo problem*, *Journal of Physics C: Solid State Physics* **3** (1970), no. 12 2436.
- [104] K. G. Wilson, *The renormalization group: Critical phenomena and the kondo problem*, *Reviews of modern physics* **47** (1975), no. 4 773.

- [105] R. Bulla, T. A. Costi, and T. Pruschke, *Numerical renormalization group method for quantum impurity systems*, *Reviews of Modern Physics* **80** (2008), no. 2 395.
- [106] K. Chen and C. Jayaprakash, *The kondo effect in pseudo-gap fermi systems: a renormalization group study*, *Journal of Physics: Condensed Matter* **7** (1995), no. 37 L491.
- [107] F. B. Anders and A. Schiller, *Spin precession and real-time dynamics in the kondo model: Time-dependent numerical renormalization-group study*, *Physical Review B* **74** (2006), no. 24 245113.
- [108] A. Weichselbaum and J. von Delft, *Sum-rule conserving spectral functions from the numerical renormalization group*, *Physical review letters* **99** (2007), no. 7 076402.
- [109] R. Bulla, A. C. Hewson, and T. Pruschke, *Numerical renormalization group calculations for the self-energy of the impurity anderson model*, *Journal of Physics: Condensed Matter* **10** (1998), no. 37 8365.
- [110] W. C. Oliveira and L. N. Oliveira, *Generalized numerical renormalization-group method to calculate the thermodynamical properties of impurities in metals*, *Physical Review B* **49** (1994), no. 17 11986.
- [111] R. Bulla, N.-H. Tong, and M. Vojta, *Numerical renormalization group for bosonic systems and application to the sub-ohmic spin-boson model*, *Physical review letters* **91** (2003), no. 17 170601.
- [112] R. Žitko and T. Pruschke, *Energy resolution and discretization artifacts in the numerical renormalization group*, *Physical Review B* **79** (2009), no. 8 085106.
- [113] A. K. Mitchell, M. R. Galpin, S. Wilson-Fletcher, D. E. Logan, and R. Bulla, *Generalized wilson chain for solving multichannel quantum impurity problems*, *Physical Review B* **89** (2014), no. 12 121105.
- [114] S.-S. B. Lee, F. B. Kugler, and J. von Delft, *Computing local multipoint correlators using the numerical renormalization group*, *Physical Review X* **11** (2021), no. 4 041007.
- [115] J. B. Rigo and A. K. Mitchell, *Automatic differentiable numerical renormalization group*, *Physical Review Research* **4** (2022), no. 1 013227.
- [116] “Sometimes Eqs. A.17 and A.18 are written to include a rescaling of  $H_N$  at each step  $N$  [105], but we omit those factors here for brevity..”
- [117] P. Nozieres and A. Blandin, *Kondo effect in real metals*, *Journal de Physique* **41** (1980), no. 3 193–211.

- [118] A. O. Gogolin, *On the theory of the Kondo effect in two-dimensional metals*, *Zeitschrift für Physik B Condensed Matter* **92** (mar, 1993) 55–59.
- [119] A. K. Zhuravlev and V. Y. Irkhin, *Kondo effect in the presence of van hove singularities: A numerical renormalization group study*, *Physical Review B* **84** (dec, 2011) 245111.
- [120] A. Zhuravlev, A. Anokhin, and V. Y. Irkhin, *One-and two-channel kondo model with logarithmic van hove singularity: A numerical renormalization group solution*, *Physics Letters A* **382** (2018), no. 7 528–533.
- [121] D. E. Logan, A. P. Tucker, and M. R. Galpin, *Common non-fermi liquid phases in quantum impurity physics*, *Physical Review B* **90** (2014), no. 7 075150.
- [122] A. K. Mitchell, M. Vojta, R. Bulla, and L. Fritz, *Quantum phase transitions and thermodynamics of the power-law Kondo model*, *Physical Review B* **88** (nov, 2013) 195119.
- [123] C. Gonzalez-Buxton and K. Ingersent, *Renormalization-group study of Anderson and Kondo impurities in gapless fermi systems*, *Phys. Rev. B* **57** (Jun, 1998) 14254–14293.
- [124] M. Vojta and L. Fritz, *Upper critical dimension in a quantum impurity model: Critical theory of the asymmetric pseudogap Kondo problem*, *Phys. Rev. B* **70** (Sep, 2004) 094502.
- [125] L. Fritz and M. Vojta, *Phase transitions in the pseudogap anderson and Kondo models: Critical dimensions, renormalization group, and local-moment criticality*, *Phys. Rev. B* **70** (Dec, 2004) 214427.
- [126] P. Igoshev and V. Y. Irkhin, *Giant van hove density of states singularities and anomalies of electron and magnetic properties in cubic lattices*, *Physics of Metals and Metallography* **120** (2019) 1282–1290.
- [127] P. Igoshev and V. Y. Irkhin, *Giant density-of-states van hove singularities in the face-centered cubic lattice*, *Physics Letters A* **438** (2022) 128107.
- [128] A. Chandrasekaran and J. J. Betouras, *A practical method to detect, analyze, and engineer higher order van hove singularities in multi-band hamiltonians*, *Advanced Physics Research* (2023).